Article

Cell

Mutational Landscape of Secondary Glioblastoma Guides MET-Targeted Trial in Brain Tumor

Graphical Abstract

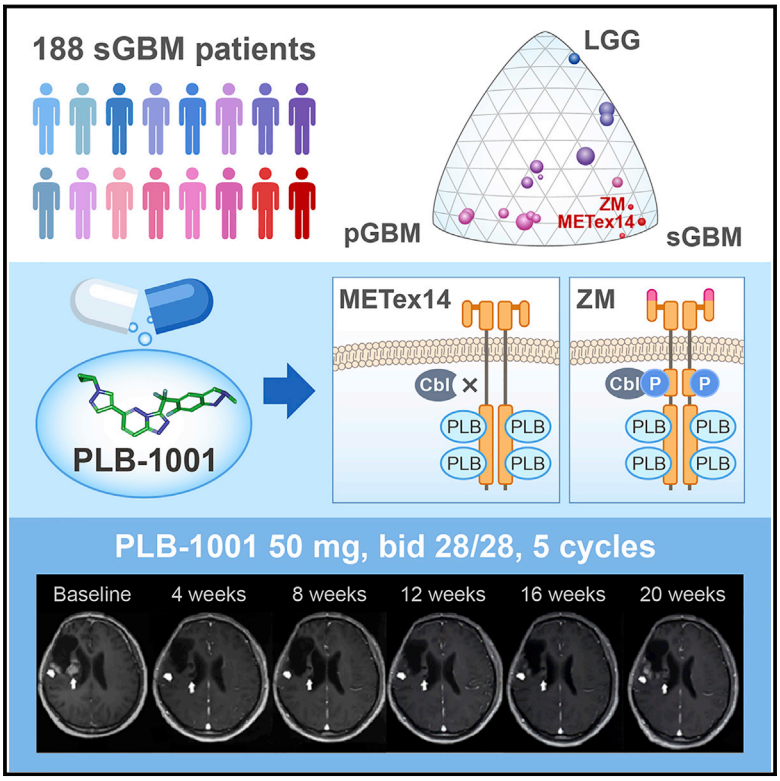

Highlights

- Characterization of the mutational landscape of secondary glioblastoma
- Clonal and subclonal *MET*ex14 promote glioma progression and mark worse prognosis
- PLB-1001 is a highly selective, efficient, and BBB-permeable MET kinase inhibitor
- PLB-1001 provides a safe and efficacious therapeutic approach for glioma treatment

Authors

Huimin Hu, Quanhua Mu, Zhaoshi Bao, ..., Xiaolong Fan, Jiguang Wang, Tao Jiang

Correspondence

xfan@bnu.edu.cn (X.F.),
jgwang@ust.hk (J.W.),
taojiang1964@163.com (T.J.)

In Brief

A new MET inhibitor shows preliminary efficacy for treatment of patients with secondary glioblastoma.

Hu et al., 2018, Cell *175*, 1–14
November 29, 2018 © 2018 Elsevier Inc.
https://doi.org/10.1016/j.cell.2018.09.038

CellPress

Please cite this article in press as: Hu et al., Mutational Landscape of Secondary Glioblastoma Guides MET-Targeted Trial in Brain Tumor, Cell (2018), https://doi.org/10.1016/j.cell.2018.09.038

Article

Cell

Mutational Landscape of Secondary Glioblastoma Guides MET-Targeted Trial in Brain Tumor

Huimin Hu,[1,14] Quanhua Mu,[2,12,14] Zhaoshi Bao,[1,4,14] Yiyun Chen,[3,12,14] Yanwei Liu,[1,5,14] Jing Chen,[1] Kuanyu Wang,[1] Zheng Wang,[1] Yoonhee Nam,[3] Biaobin Jiang,[2,3,13] Jason K. Sa,[10] Hee-Jin Cho,[10] Nam-Gu Her,[10] Chuanbao Zhang,[4] Zheng Zhao,[1] Ying Zhang,[1] Fan Zeng,[1] Fan Wu,[1] Xun Kang,[6] Yuqing Liu,[1] Zenghui Qian,[1] Zhiliang Wang,[1] Ruoyu Huang,[1] Qiangwei Wang,[1] Wei Zhang,[4] Xiaoguang Qiu,[5] Wenbin Li,[6] Do-Hyun Nam,[10,11] Xiaolong Fan,[7,*] Jiguang Wang,[2,3,12,*] and Tao Jiang[1,4,8,9,15,*]

[1]Beijing Neurosurgical Institute, Capital Medical University, 100050 Beijing, China
[2]Department of Chemical and Biological Engineering, The Hong Kong University of Science and Technology, Hong Kong, China
[3]Division of Life Science, The Hong Kong University of Science and Technology, Hong Kong, China
[4]Department of Neurosurgery, Beijing Tiantan Hospital, Capital Medical University, 100050 Beijing, China
[5]Department of Radio-therapy, Beijing Tiantan Hospital, Capital Medical University, 100050 Beijing, China
[6]Department of Oncology, Beijing Shijitan Hospital, Capital Medical University, 100050 Beijing, China
[7]Laboratory of Neuroscience and Brain Development, Beijing Key Laboratory of Gene Resource and Molecular Development, Beijing Normal University, 100875 Beijing, China
[8]Center of Brain Tumor, Beijing Institute for Brain Disorders, 100069 Beijing, China
[9]China National Clinical Research Center for Neurological Diseases, 100050 Beijing, China
[10]Institute for Refractory Cancer Research, Samsung Medical Center, Seoul, Korea
[11]Department of Neurosurgery, Samsung Medical Center, Sungkyunkwan University School of Medicine, Seoul, Korea
[12]Center of Systems Biology and Human Health, The Hong Kong University of Science and Technology, Hong Kong, China
[13]Institute for Advanced Study, The Hong Kong University of Science and Technology, Hong Kong, China
[14]These authors contributed equally
[15]Lead Contact
*Correspondence: xfan@bnu.edu.cn (X.F.), jgwang@ust.hk (J.W.), taojiang1964@163.com (T.J.)
https://doi.org/10.1016/j.cell.2018.09.038

SUMMARY

Low-grade gliomas almost invariably progress into secondary glioblastoma (sGBM) with limited therapeutic option and poorly understood mechanism. By studying the mutational landscape of 188 sGBMs, we find significant enrichment of *TP53* mutations, somatic hypermutation, *MET*-exon-14-skipping (*MET*ex14), *PTPRZ1-MET* (ZM) fusions, and *MET* amplification. Strikingly, *MET*ex14 frequently co-occurs with ZM fusion and is present in ~14% of cases with significantly worse prognosis. Subsequent studies show that *MET*ex14 promotes glioma progression by prolonging MET activity. Furthermore, we describe a MET kinase inhibitor, PLB-1001, that demonstrates remarkable potency in selectively inhibiting *MET*-altered tumor cells in preclinical models. Importantly, this compound also shows blood-brain barrier permeability and is subsequently applied in a phase I clinical trial that enrolls *MET*-altered chemo-resistant glioma patients. Encouragingly, PLB-1001 achieves partial response in at least two advanced sGBM patients with rarely significant side effects, underscoring the clinical potential for precisely treating gliomas using this therapy.

INTRODUCTION

According to the World Health Organization (WHO) classification of tumors of the CNS, malignant adult diffused gliomas are classified into grades II to IV based on histologic features (Louis et al., 2016). Grade IV gliomas, or glioblastoma (GBM), can be further classified into primary GBM (pGBM) and secondary GBM (sGBM) (Wen and Kesari, 2008). Mostly *IDH* wild-type, pGBM is *de novo* developed and commonly found in the elderly. In contrast, sGBM typically affects younger patients and progresses from low-grade diffuse astrocytoma or oligodendroglioma within 5–10 years of diagnosis (Louis et al., 2016). The limitations in current chemotherapy using temozolomide (TMZ), which functions by nonselective DNA damage, includes side effects and chemo-resistance. Under this therapy, almost all patients will recur, and the recurrent tumors usually carry distinct alterations that might lead to drug-resistance (Wang et al., 2016). To improve glioma treatment, it is essential to identify new oncogenic alterations and design therapies to specifically target them.

Although the mutational (Brennan et al., 2013; Ceccarelli et al., 2016; Brat et al., 2015) and evolutionary landscapes (Lee et al., 2017; Wang et al., 2016) of GBM have been well studied, the genomic and transcriptomic features and evolution mechanisms of the progression from LGG to sGBM remain elusive. Recent longitudinal studies that collected paired LGG and sGBM samples illustrated the roles of PI3K/Akt/mTOR pathway, RB pathway (Bai et al., 2016; Johnson et al., 2014),

cell-cycle regulations (Mazor et al., 2015), and DNA methylation reprogramming (Mazor et al., 2017) during glioma progression. However, all of these studies enrolled <20 sGBM patients, which limits the statistical power. To date, actionable solutions have rarely been provided. Thus, a large-scale retrospective and prospective investigation is required to reveal the mutational landscape of sGBM and to seek approaches of translating these findings into clinical practice.

Here, we describe an integrated genomic and transcriptomic analysis of 188 sGBM patients and reveal the comprehensive mutational landscape of sGBM. Comparing the profile of sGBM with that of LGG and pGBM, we found that *MET* alterations, including *MET* exon 14 skipping (*MET*ex14) and *PTPRZ1-MET* (ZM) fusion, are highly enriched in sGBM. Functional studies of *MET* alterations in cell lines and xenografts demonstrated hyper-activation of MET signaling pathway and acceleration of tumor proliferation. In addition, we investigated the microenvironment and showed the enrichment of tumor-associated macrophages in patients with both *MET*ex14 and ZM fusion. A MET-specific inhibitor, PLB-1001, was then characterized and demonstrated effective suppression of MET-induced glioma progression in cell lines and xenografts. Finally, in an open-label phase I clinical trial, we demonstrated the safety and efficacy of PLB-1001 in patient treatment. Taken together, we described a comprehensive somatic mutation landscape of sGBM and provided a MET-targeted therapy for precision neuro-oncology.

RESULTS

Mutational Landscape of sGBM

To reveal the mutational landscape of sGBM, we collected and integrated genomic and/or transcriptomic data from 188 sGBM patients (Table S1), including 104 newly collected samples from the Chinese Glioma Genome Atlas (CGGA), 4 newly collected samples from the Samsung Medical Center (SMC), and previously published resources (Bao et al., 2014; Brennan et al., 2013; Johnson et al., 2014; Kim et al., 2015a, 2015b; McLendon et al., 2008; Parsons et al., 2008; Suzuki et al., 2015; Wang et al., 2016) (Figure S1A; Table S1; STAR Methods). The landscape of somatic mutations of 145 patients with DNA sequencing (i.e., whole genome, whole exome, or targeted sequencing) revealed mutations and/or deletions in *TP53*, *ATRX*, *CIC*, *FUBP1*, *CDKN2A*, *RB1*, and PTEN-PI3K pathway and mutations and/or amplifications in *MET*, *EGFR*, *PDGFRA*, and *CDK4* (Figure 1A). In 78 patients with RNA sequencing data, *MET*ex14 was detected in 14% (95% confidence interval [CI], 8.0%–23.5%) of sGBM cases (Figures S1B and S1C). Sanger sequencing validated this event in patients with available samples (Figure S1D). Additionally, various ZM fusions were identified in four sGBM cases (5% with 95% CI, 2.6%–7.6%), all of which simultaneously harbor *MET*ex14 (Figure 1A). Missense mutations on Arg132 of *IDH1* were observed in 67% of sGBMs, similar as reported previously (Nobusawa et al., 2009; Ohgaki and Kleihues, 2013). The *IDH1* mutation status showed no association with *MET*ex14 alteration ($p > 0.5$, Fisher's exact test). Not surprisingly, we found mutations in *TP53*, *ATRX*, *CIC*, and *FUBP1* were more frequent in *IDH1* mutant cases, while *PTEN* and *EGFR* mutations were enriched in *IDH1* wild-type cases ($p < 0.05$ by Fisher's exact test, Figure S1E). In addition, by integrating data across platforms (STAR Methods), we identified 18 hypermutated cases out of 142 sGBM patients in Asian populations and 13 out of 39 in Caucasian population (Figure S1F). Hypermutation was found to be higher in Caucasian population and closely associated with TMZ treatment (Table S1).

Divergence of sGBM from Low-Grade Glioma and Primary GBM

To systematically compare LGG, pGBM, and sGBM, we characterized genomic alterations of the sGBM cohort and acquired genomic data of pGBM and LGG from The Cancer Genome Atlas (TCGA) (Brennan et al., 2013; Ceccarelli et al., 2016). We observed in pGBM a higher frequency of alterations in *EGFR*, *PTEN*, *PDGFRA*, *CDK4*, *CDKN2A*, *PIK3CA*, and *RB1* (Brennan et al., 2013) (left corner at Figure 1B; Table S2). As expected, alterations in *CIC*, *FUBP1*, *TP53*, *ATRX*, and *IDH1* were more common in LGG and sGBM. Particularly, *IDH1* mutations were observed in 77% of LGG, 67% of sGBM, but only 5% of pGBM. Hypermutation was found in 16% of sGBM, which was comparable with recurrent GBM (17%) (Wang et al., 2016). Additionally, higher frequencies of alterations in *MTOR*, *NF1*, *RB1* (Bai et al., 2016; Johnson et al., 2014), and *MET* were observed in sGBMs over LGG (Table S2), suggesting that they were potentially related to the progression of LGG. Interestingly, *MET*ex14, ZM, and *MET* amplification were significantly enriched in sGBM ($p = 4.0 \times 10^{-7}$, 1.2×10^{-2}, and 2.0×10^{-4} by Fisher's exact test, Figure 1B). Remarkably, the frequency of *MET*ex14 in sGBM (11/78) was significantly higher than those in LGG (6/530, $p = 5.3 \times 10^{-7}$) and pGBM (3/174, $p = 2.3 \times 10^{-4}$, Fisher's exact test, Figure 1C). By defining sGBM overall survival (OS) as the period from the first diagnosis of sGBM until patient death (Figure 1D), we observed that sGBM patients with *MET*ex14 showed significantly poorer OS compared to those without *MET*ex14 (Figure 1E), suggesting that *MET*ex14 was a prognostic marker for glioma patients.

*MET*ex14 Promotes MET Signaling Hyper-activation and Glioma Progression

Various genomic mutations were observed in patients with exon 14 skipping on *MET* transcript (deletion of entire exon 14 in Figure 2A, disruption of its splice donor site in Figure S2A). *MET* exon 14 encodes the juxta-membrane (JM) domain on MET, which contains the phosphorylation site Tyr1003 (Y1003) required for c-Cbl-mediated ubiquitination and degradation of MET. Therefore, *MET*ex14 results in prolonged stability and constitutive activation of MET (Frampton et al., 2015) (Figure 2B). In *MET*ex14-positive samples, we observed elevated expression of *MET* transcript (Figure S2B). The degradation signal marked by JM domain Y1003 phosphorylation, however, was abolished by *MET*ex14 (Figure 2C), which leads to reduced MET degradation. As STAT3 acts downstream of MET signaling and plays essential roles in MET-mediated tumorigenesis (Zhang et al., 2002), we examined the effects of *MET* alterations on STAT3 activation. Immunohistochemistry (IHC) and histology staining of paired LGG and progressed sGBM samples (P068) with both ZM fusion and *MET*ex14

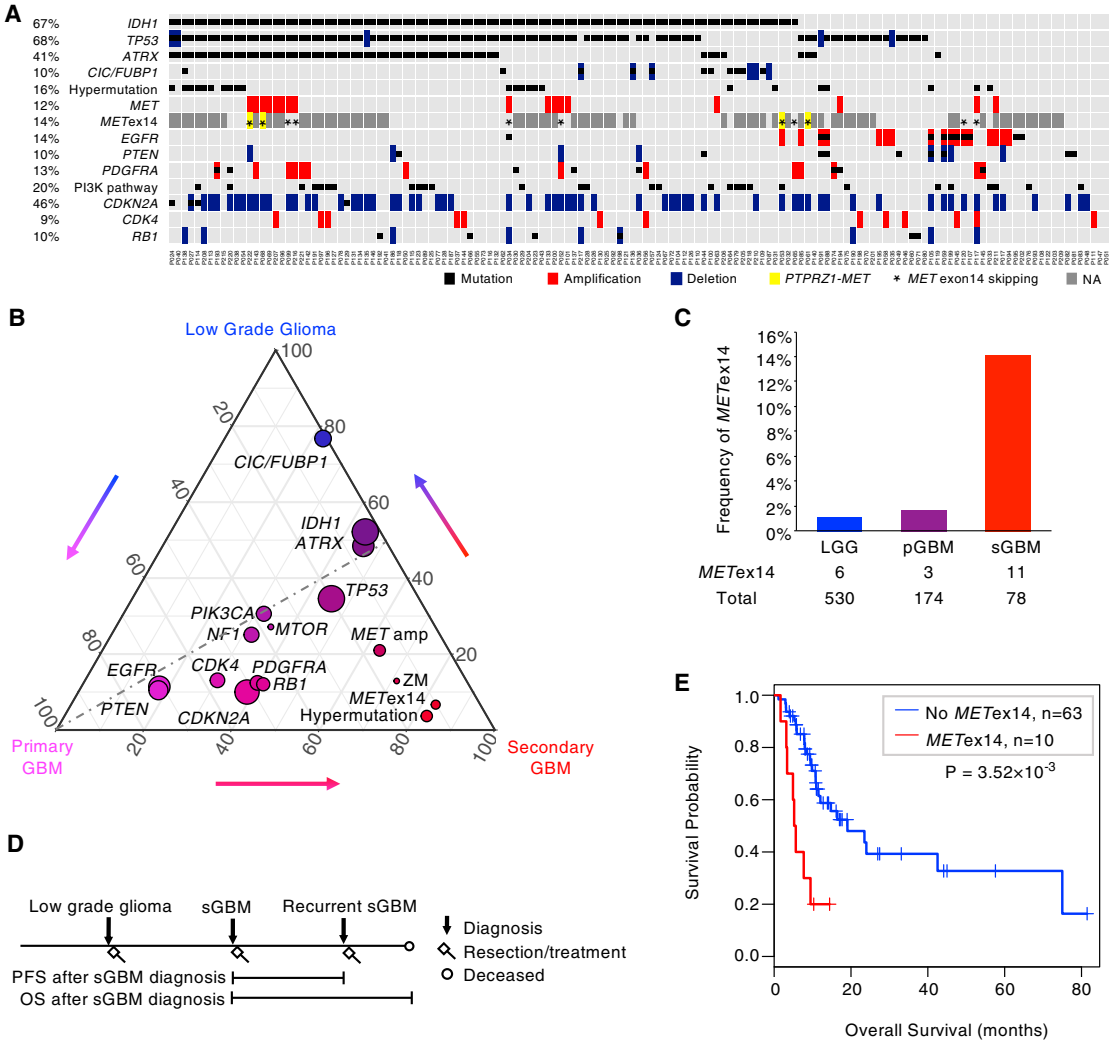

Figure 1. Mutational Landscape of Secondary Glioblastoma

(A) Mutational landscape of 145 sGBMs. Alterations in common driver genes are displayed. *MET*ex14 and *MET* fusion in cases without RNA sequencing data are marked as NA (not available). The incidence of all alterations is listed on the left.

(B) Ternary plot of mutation frequency in driver genes, comparing pGBM (left, magenta), sGBM (right, red), and LGG (top, blue). The color of each node indicates relative frequency of mutations in LGG, pGBM, and sGBM, whereas the node size represents their overall frequency in glioma.

(C) Frequencies of *MET*ex14 in LGG (blue, n = 530), pGBM (purple, n = 174), and sGBM (red, n = 78).

(D) Description of the definition of progression-free survival (PFS) and overall survival (OS) in sGBM patients.

(E) Overall survival of sGBM patients with and without *MET*ex14. None of the patients included in this analysis had received MET-targeted therapy.

See also Figure S1 and Tables S1 and S2.

demonstrated hyper-activation of MET/STAT3 signaling pathway and elevated proliferation and angiogenesis activities while progressing into the *MET*ex14-positive sGBM (Figure 2D). Moreover, *MET*ex14 expression is dramatically elevated during LGG progression in 3 out of 4 patients who have longitudinal sequencing samples (Figure 2E). Thus, we hypothesize that subclones harboring these mutations are positively selected and fast proliferating during tumor progression. In agreement with our hypothesis, sGBMs with *MET*ex14 at clonal and subclonal level both showed significantly poorer OS compared to *MET*ex14-negative patients (Figure S2C), indicating that the clonal expansion of *MET*ex14 might contribute to shortened patient survival.

Characterization of Different *MET* Alterations

By integrating all 782 glioma patients (combined cohort of sGBM, pGBM, and LGG), we discovered a strong tendency of *MET*ex14 and ZM fusion to co-occur ($p < 1.0 \times 10^{-4}$ by Fisher's exact test, Figure 3A). Cloning the full-length ZM fusion transcript from the cDNA library of sGBM, we found intact *MET* exon 14 on the same transcript, suggesting that *MET* fusion and *MET*ex14 probably occur on different copies of *MET* in

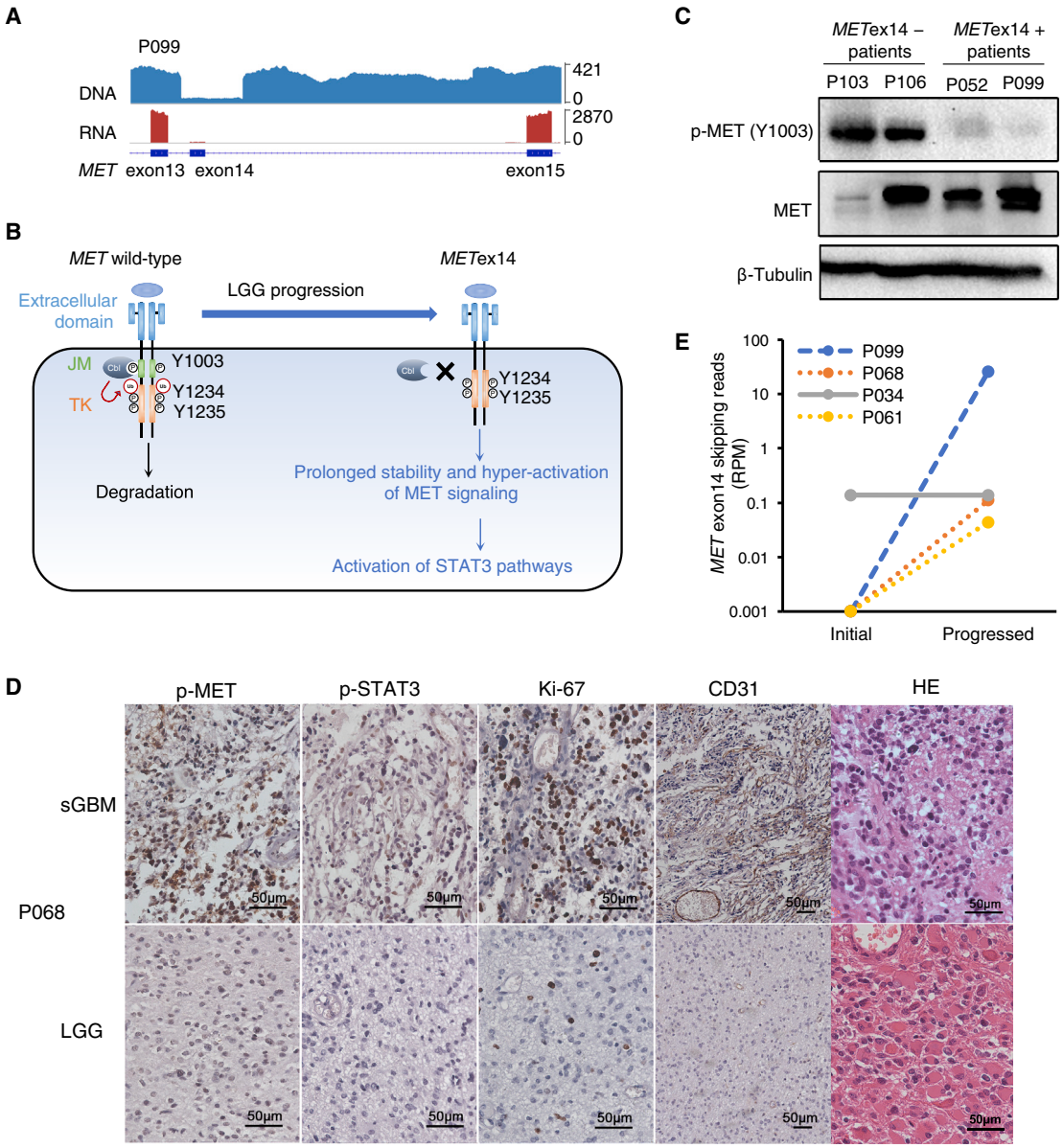

Figure 2. *MET* Exon 14 Skipping Promotes *MET* Overexpression and Hyperactivation of MET Signaling

(A) Deletion of *MET*ex14 in patient P099 is observed in both DNA and RNA level. The break points in DNA are chr7:116410812-116412364. Y axes are the number of reads in whole-genome sequencing and RNA sequencing, respectively.

(B) Mechanism of *MET*ex14 in regulating MET signaling and promoting glioma progression. Upon the binding of MET extracellular domain with its ligand, HGF, the MET receptor dimerizes and undergoes *trans*-autophosphorylation in the cytoplasmic domains. Phosphorylation of Y1234 and Y1235 on the MET kinase domain leads to the activation of MET and its downstream signaling pathways, while phosphorylation at Y1003 on the juxta-membrane (JM) domain negatively regulate MET signaling by promoting c-Cbl-mediated ubiquitination and degradation of MET. By skipping the JM domain encoded by exon 14, *MET*ex14 alteration results in prolonged stabilization of MET receptor and hyper-activation of MET signaling and downstream pathways.

(C) Western blotting of total MET and phosphorylated MET of Y1003 on the JM domain in *MET*ex14-negative samples and *MET*ex14-positive samples.

(D) Immunohistochemistry and histopathology analysis of the initial *MET* wild-type low-grade glioma (LGG) and the progressed sGBM in patient P068, which contains both *MET*ex14 and E8-E2 ZM fusion variant.

(E) Number of *MET* exon 14 skipping reads in 4 patients with paired initial LGG and progressed sGBM available. RPM, reads per million.

See also Figure S2.

the genome, resulting in the production of MET protein with either PTPRZ1 chimera sequence at its N-terminal or with skipped JM domain (Figure S3A; Data S1). To examine the dysregulated gene expression profiles associated with different *MET* alterations, we compared *MET* wild-type sGBM samples with those harboring *MET*ex14 and those harboring ZM fusions,

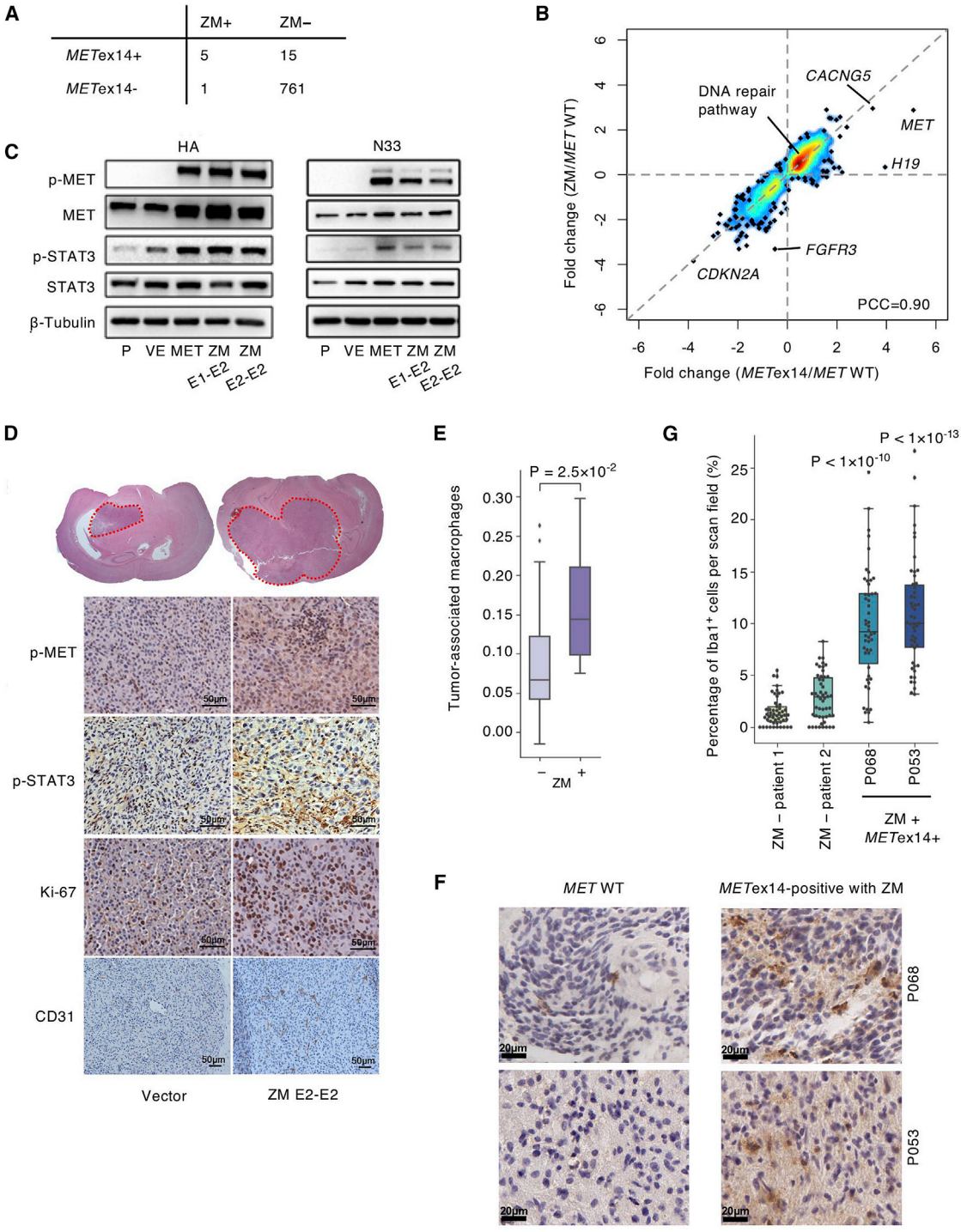

Figure 3. Characterization of Different *MET* Alterations

(A) Contingency table of *MET*ex14 and ZM fusion in glioma. GBM and LGG cohorts from TCGA are also included.

(B) Fold changes of differentially expressed genes in sGBM samples with *MET*ex14 and/or ZM fusion, compared to sGBMs with wild-type *MET*. PCC, Pearson correlation coefficient.

(C) Western blotting of total MET, activated MET (p-MET, with phosphorylation of Y1234/Y1235 on the kinase domain), total STAT3, and activated STAT3 (p-STAT3, with phosphorylation of Y507) in HA and N33 cells transduced with *MET* and ZM fusion (E1-E2 and E2-E2 variants).

(D) Staining of activated MET (p-MET), activated STAT3 (p-STAT3), Ki-67, and CD31 in the intracranial tumors formed by U87 MG cells stably expressing ZM fusion (ZM E2-E2) or with the vector control.

(legend continued on next page)

respectively. As a result, 1,453 genes were found to be differentially expressed in *MET*ex14- or ZM-positive sGBM, with more genes upregulated than downregulated in both groups. *MET*, *H19*, *CACNG5*, and genes in DNA repair pathway showed elevated expression in both *MET*ex14- and ZM-positive samples, while *FGFR3* and *CDKN2A* were downregulated. The fold change of the differentially expressed genes in *MET*ex14-positive and in ZM-positive samples were highly correlated (Pearson's correlation coefficient = 0.90), indicating similar effects of *MET*ex14 and ZM on gene expression (Figure 3B).

We further assessed the oncogenic effects of *MET* alterations on glioma cells by generating human astrocyte (HA) and patient-derived *IDH* wild-type GBM (N33) cell lines that overexpress *MET* or ZM fusions using adenovirus transduction. Expression of both *MET* and ZM fusions resulted in hyper-activation of MET and STAT3 signaling (Figure 3C). Furthermore, the U87 MG cells with lentivirus-mediated ZM expression had a higher cell proliferation rate (Figure S3B). On the xenograft model generated by subcutaneous implantation in BALB/c nude mice, tumors of U87 MG cells overexpressing the ZM fusion grew more rapidly than did tumors formed by cells transduced with control vector (Figure S3C, $p = 2.0 \times 10^{-3}$). The same U87 MG cells stably expressing the ZM fusion were also injected into the brains of BALB/c nude mice. Tumors derived from ZM-harboring U87 MG cells grew more rapidly as shown by magnetic resonance imaging (MRI) examination at 30 days after transplantation (Figure S3D), resulting in significantly poorer OS ($p = 4.0 \times 10^{-4}$, Figure S3E). Immunostaining showed higher level of activation of MET and STAT3 signaling in intracranial tumors harboring ZM fusion than in tumors without ZM fusion (Figure 3D).

Tumor-associated macrophages are known to be highly abundant in high-grade glioma, where they promote tumor proliferation, invasion, angiogenesis, and suppress immune responses (Hambardzumyan et al., 2016). Comparing sGBM with LGG and pGBM samples, we observed more enriched tumor-associated macrophages in sGBM compared to LGG, but less enriched in sGBM compared to pGBM (Figure S3F). Moreover, in sGBM patients, elevated number of macrophages was also identified in *MET*ex14-positive sGBM that co-occurred with ZM fusions (Figures 3E and S3G). We validated this observation by IHC staining of a macrophage marker, IBA1, on two sGBM samples with *MET*ex14 and ZM fusion as well as two control samples without any *MET* alterations (Figure 3F). Quantifying the percentage of IBA1 staining-positive cells in randomly selected scan fields from each sample, significantly higher fraction of macrophages were observed in sGBM with concurrent *MET*ex14 and ZM fusion (Figure 3G), suggesting that *MET* alterations may contribute to tumor malignancy by recruiting tumor-associated macrophages and altering the glioma microenvironment. Thus, our analysis suggests the diverse roles of *MET* alterations in glioma progression by activating MET signaling, promoting tumor growth, and altering the tumor microenvironment.

PLB-1001 Is a Highly Selective MET Inhibitor with Blood-Brain Barrier Permeability

Several MET inhibitors have been developed, yet insufficient induction of tumor regression and rapid development of acquired resistance remain unresolved challenges in MET inhibitor-mediated cancer therapies (Bender et al., 2016; Gherardi et al., 2012; Lai et al., 2014). Four MET inhibitors, crizotinib (a dual-targeted inhibitor of MET and ALK kinases) (Cui et al., 2011), cabozantinib, foretinib, and INCB28060, and 56 non-MET inhibitors were applied to a ZM-positive and a *MET*ex14-positive patient-derived glioma cell line, respectively, to test the sensitivity of the cell lines to the drugs (STAR Methods). MET inhibitors demonstrated significantly better growth inhibition effects than non-MET-inhibitors on the both cell lines (Wilcoxon rank-sum test, $p = 4.0 \times 10^{-3}$, Figure S3H; and $p = 9.0 \times 10^{-4}$, Figure S3I), suggesting good potential of MET inhibitors to treat gliomas with *MET* alterations.

We described a highly selective ATP-competitive small-molecule MET inhibitor, PLB-1001 (Figure 4A; STAR Methods). To elucidate the molecular structure of PLB-1001 in complex with its target, we performed molecular dynamics simulation using the tyrosine kinase domain structure of MET as the starting model (Figure 4A). PLB-1001 binds to the conventional ATP-binding pocket of the tyrosine kinase superfamily. Similar to the structure of the complex formed by crizotinib with the same domain (Cui et al., 2011), PLB-1001 occupied the bulk of the ATP-binding pocket. However, the cyclopropyl moiety of PLB-1001 was trapped into the hydrophobic groove that was formed by the side chains of Ile1084, Tyr1159, Met1211, and Asp1164. Moreover, the indazol moiety of PLB-1001 bound to another cleft, which was formed by the side chains of Asp1204, Arg1208, Pro1246, and the main chain atoms of Gly1224 and Asp1228. In contrast, these two binding pockets were not involved in the stabilization of crizotinib. Of note, the piperidine moiety of crizotinib clearly pointed toward the solvent and did not interact with the kinase molecule. The additional interactions of PLB-1001 with the kinase indicated a higher binding affinity and a better inhibition effect compared with crizotinib. To test the selectivity of PLB-1001, LANCE enzyme assays were performed to test the efficiency of PLB-1001 in inhibiting 100 kinases through detection of the level of ULight/CREBtide-substrate phosphorylation after incubation with 2 μM of PLB-1001 (Table S3; STAR Methods). The kinase inhibition assay showed that PLB-1001 inhibited MET activity

(E) Tumor-associated macrophages in patients harboring the *MET*ex14 and ZM fusion (n = 4) compared to patients with wild-type *MET* (n = 74) by CIBERSORT ($p = 2.5 \times 10^{-2}$ by Wilcoxon rank-sum test). The box shows the quartiles of the dataset while the whiskers extend to show the rest of the distribution.

(F) Immunohistochemistry staining of two ZM-negative samples and two *MET*ex14-positive sGBM with ZM fusion (P068 and P053) with antibody against macrophage marker Iba1. Scale bars, 20 μm.

(G) Percentage of $Iba1^+$ cells per scan field was quantified from immunohistochemistry staining. Fifty scan fields were randomly selected from each patient (5 whole-slide imaging per patient, 10 randomly selected scan fields per image). p value of sGBM samples harboring *MET* alterations was calculated by Wilcoxon rank-sum test against two *MET* wild-type samples. The box shows the quartiles of the dataset while the whiskers extend to show the rest of the distribution.

See also Figure S3 and Data S1.

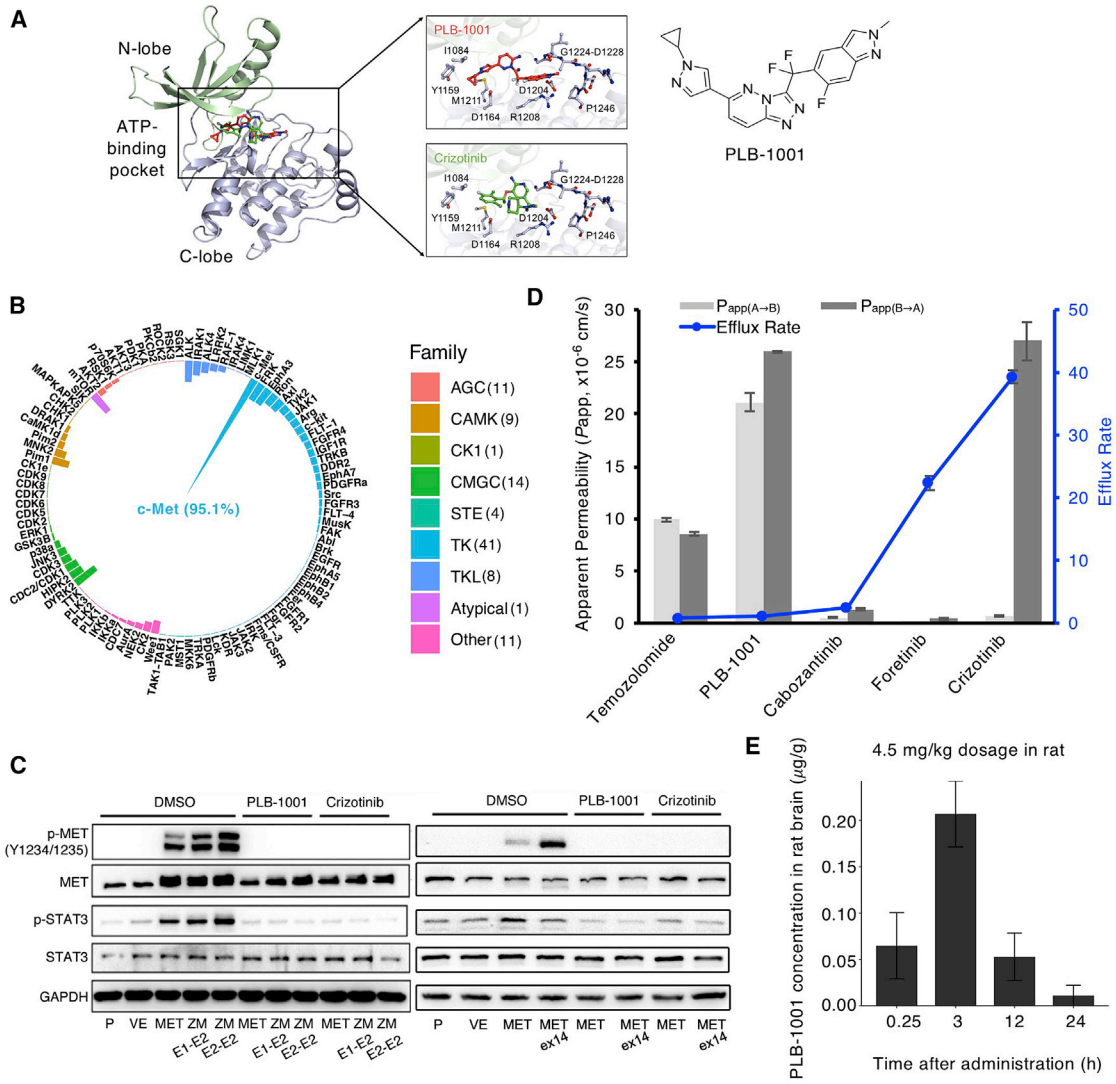

Figure 4. MET Inhibitor, PLB-1001, with Improved Selectivity, Potency, and Blood-Brain Barrier Permeability

(A) Molecular dynamics simulation of PLB-1001 bound to ATP-binding pocket of MET kinase domain (PDB: 2WGJ) and comparison with the complex structure of MET kinase domain (PDB: 2WGJ) and crizotinib. Details of the interaction of kinase domain with PLB-1001 (red, chemical structure shown on the right) and crizotinib (green) are highlighted in the box.

(B) Inhibition rates of 100 kinases by PLB-1001. The kinases assayed are colored according to different kinase families in the human kinome.

(C) Western blotting of total MET, activated MET (p-MET Y1234/1235), total STAT3, and activated STAT3 in human astrocytes (HA) transiently overexpressing ZM fusion (E1-E2 or E2-E2), *MET*ex14, or *MET* by adenoviral vectors versus parental cell (P) or vector control (VE) under PLB-1001 treatment (30 μM, 6 hr), crizotinib treatment (3 μM, 6 hr), or DMSO control.

(D) MDCK-MDR1 cell permeability assay demonstrating the permeability (left axis represented by the bar plot) and efflux rate (right axis represented by the blue line) of temozolomide, PLB-1001, cabozantinib, crizotinib, and foretinib. Data are presented as means ± SD.

(E) PLB-1001 concentration in rat brain following intragastric administration of 4.5 mg/kg body weight of PLB-1001 (n = 6). Data are presented as means ± SD. See also Figure S3 and Tables S3 and S4.

by 95.1%, whereas other kinases, including kinases in the same family as MET (Manning et al., 2002), were barely inhibited, confirming the high selectivity of PLB-1001 for MET kinase (Figure 4B; list of assayed kinases in Table S3). To test the efficacy of PLB-1001 in targeting *MET* alterations, human astrocytes expressing exogenous ZM fusion or *MET*ex14 were used. Similar with crizotinib, PLB-1001 inhibited the phosphorylation of MET and STAT3, indicating a robust inhibitory effect of PLB-1001 on MET and its downstream signaling pathways (Figure 4C).

We then employed the MDCK (Madin-Darby canine kidney)-MDR1 cell line (Cecchelli et al., 2007) to compare the permeability and efflux rate of PLB-1001, temozolomide, and three other MET-targeted drugs (crizotinib, cabozantinib, and foretinib). The apparent permeability and efflux rate of each drug was calculated from the liquid chromatography-tandem mass

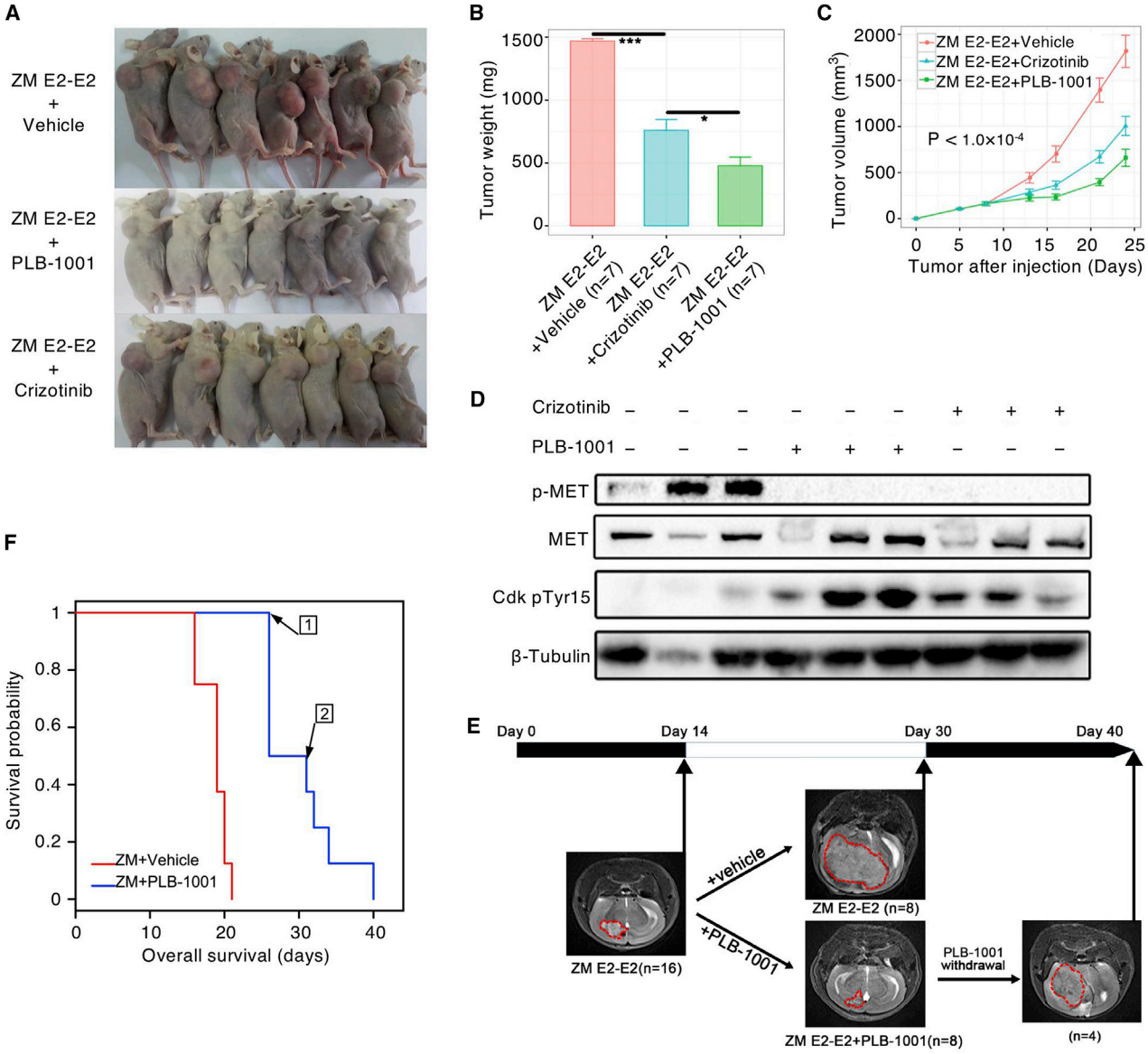

(legend on next page)

spectrometry (LC-MS/MS)-detected drug concentration across the MDCK-MDR1 cell monolayer (see STAR Methods). PLB-1001 has higher apparent permeability and lower efflux rate than other MET inhibitors (crizotinib, cabozantinib, and foretinib) in MDCK-MDR1 cell model (Figure 4D). The two essential blood-brain barrier (BBB) transporters, P-glycoprotein (P-gp) and breast cancer resistance protein (BCRP), do not bind and efflux PLB-1001, as the efflux rate of PLB-1001 across monolayers of the P-gp-expressing MDCK-MDR1 or the BCRP-expressing Caco-2 is similar with that of non-substrates (Figures S3J and S3K) with no significant changes in response to BCRP inhibitor treatment (Figure S3L). We then tested the PLB-1001 concentration in the brain of Sprague-Dawley rats and found a peak of 0.207 μg/g (with brain/total plasma ratio ~1.75%) of tissue weight at 3 hr after intragastric administration of 4.5 mg/kg body weight of PLB-1001 (corresponds to 50 mg *bis in die* [bid] dose in human [body weight of 70 kg]), and the concentration then declined gradually (Figure 4E; Table S4). In summary, PLB-1001 shows superior specificity in MET inhibition and is permeable in crossing the BBB in cell and rat models.

PLB-1001 Suppresses Tumor Progression Driven by *MET* Alterations

In the ZM-harboring U87 MG xenograft models, PLB-1001 and crizotinib were administered when the subcutaneous tumors reached a volume of ~100 mm^3. PLB-1001 treatment resulted in a significant reduction in the growth of ZM-harboring xenografts compared with crizotinib and vehicle (Figures 5A–5C). Furthermore, PLB-1001 and crizotinib inhibited MET phosphorylation, and increased Cdk2 pTyr15 phosphorylation (Figure 5D), indicating inhibition of MET signaling and tumor growth in the xenograft model.

Treatment of mice carrying intracranial orthotopic tumors derived from the same ZM-expressing glioma cell line with PLB-1001 from 14 days post-implantation showed suppressed tumor growth until 30 days post-implantation by MRI examination, which subsequently reverted to active growth following the withdrawal of PLB-1001 (Figure 5E). PLB-1001 treated mice showed a longer OS compared to untreated controls (Figure 5F). HE and IHC staining of the orthotopic tumors showed diminished staining intensities of p-MET, p-STAT3, Ki-67, CD31, and pHH3 following PLB-1001 treatment (Figure 5G). Together, these findings demonstrate that PLB-1001 treatment inhibited MET signaling, proliferation, and angiogenesis activities in the xenograft models with *MET* alterations.

Safety and Efficacy of PLB-1001 in Glioma Patients with *MET* Alterations

To further explore the safety and efficacy of PLB-1001 in patients, we translated these findings into the clinic. We have conducted a phase I, open-label study of PLB-1001 administered orally to recurrent high-grade gliomas patients with ZM fusion and/or *MET*ex14 (Figure 6A; STAR Methods). The aim of the 3+3 dose-escalation study is to estimate the maximum tolerated dose (MTD) and to identify the dose-limiting toxicity (DLT) and the recommended phase II dose (RP2D) for PLB-1001 single agent as well as to determine the pharmacokinetic/pharmacodynamics (PK/PD) profile. In total, 18 recurrent high-grade glioma patients (P01001–P01018), including 9 sGBMs and 9 grade III gliomas, carrying ZM fusions and/or *MET*ex14 were enrolled. These 18 patients, ranging from 31 to 66 years of age, were initially diagnosed with lower-grade glioma. At recurrence, the histopathological and molecular study after resection showed that their tumors have progressed into high-grade glioma with *MET* alterations. Routine TMZ treatment has been delivered either after recurrence or at initial diagnosis. They were enrolled into the PLB-1001 clinical trial at later tumor progression or recurrence events. In the trial, patients were treated by PLB-1001 with dosage ranging from 50 to 300 mg bid (Table S5). After single-dose treatment, PLB-1001 reached stable plasma concentration between 1,000 to 6,000 ng/mL in 24 hr (Figure 6B). The PLB-1001 concentration in the cerebrospinal fluid (CSF) collected on day 15 was ~3%–8% of that in plasma and showed an increasing trend with the drug dosage (Figure 6C). More detailed clinical characters were summarized in Table S5 and Figures 7A, S4, S5, and S6A–S6C.

The drug safety and potential adverse events (AEs) were carefully investigated (Table S5). Up to the study cutoff date, three sGBM patients withdrew from the trial because of trial-unrelated clinical events, including dysphagia, drug-unrelated tumor stroke, and pneumonia, and no DLT effects or deaths occurred. No MTD had been reached. Grade 3 AEs of hepatotoxicity were observed in two patients with grade III glioma, including increased ALT in one patient treated with 200 mg bid dosage

Figure 5. PLB-1001 Treatment Results in a Significant Reduction in the Growth of ZM-Harboring U87 MG Xenografts Compared with Crizotinib Treatment and Vehicle

(A) Images of subcutaneous U87 MG xenograft expressing the E2-E2 ZM fusion variant under treatment of vehicle, PLB-1001 (100 mg/day/kg of body weight), and crizotinib (50 mg/day/kg of body weight).

(B) Tumor weight of U87 MG xenografts under PLB-1001 treatment, crizotinib treatment, or vehicle control (***$p < 0.001$, *$p < 0.05$, t test). Data are presented as means ± SD.

(C) Growth curves of the subcutaneous U87 MG cell derived tumor stably expressing ZM fusion upon treatment with PLB-1001 or crizotinib from day 8 post-transplantation. Data are presented as means ± SD. p value is based on 2-way ANOVA.

(D) Western blot of Cdk2 Tyr15 phosphorylation, total, and activated MET in xenograft under PLB-1001 or crizotinib treatment.

(E) The schematic depiction of the timeline of PLB-1001 treatment, treatment withdrawal, and MRI examination of the intracranial tumors formed by U87 MG cells stably expressing ZM fusion (E2-E2). Representative mouse brain MRI images at the indicated time points are shown.

(F) Kaplan-Meier survival curves of the mice carrying intracranial tumors formed by ZM fusion-expressing U87 MG with or without PLB-1001 treatment. 1 indicates the time point when the four mice were sacrificed for tissue collection and immunostaining. 2 indicates the time point of PLB-1001 withdrawal. Female BALB/c nude mice were implanted in the brain with U87 MG cells expressing the ZM E2-E2 fusion (5×10^5 cells/ mouse) to form orthotopic tumors.

(G) HE staining of representative samples of intracranial tumors treated with PLB-1001. Representative immunostainings of p-MET, p-STAT3, Ki-67, CD31, and pHH3 in the PLB-1001- or vehicle-treated tumors are shown.

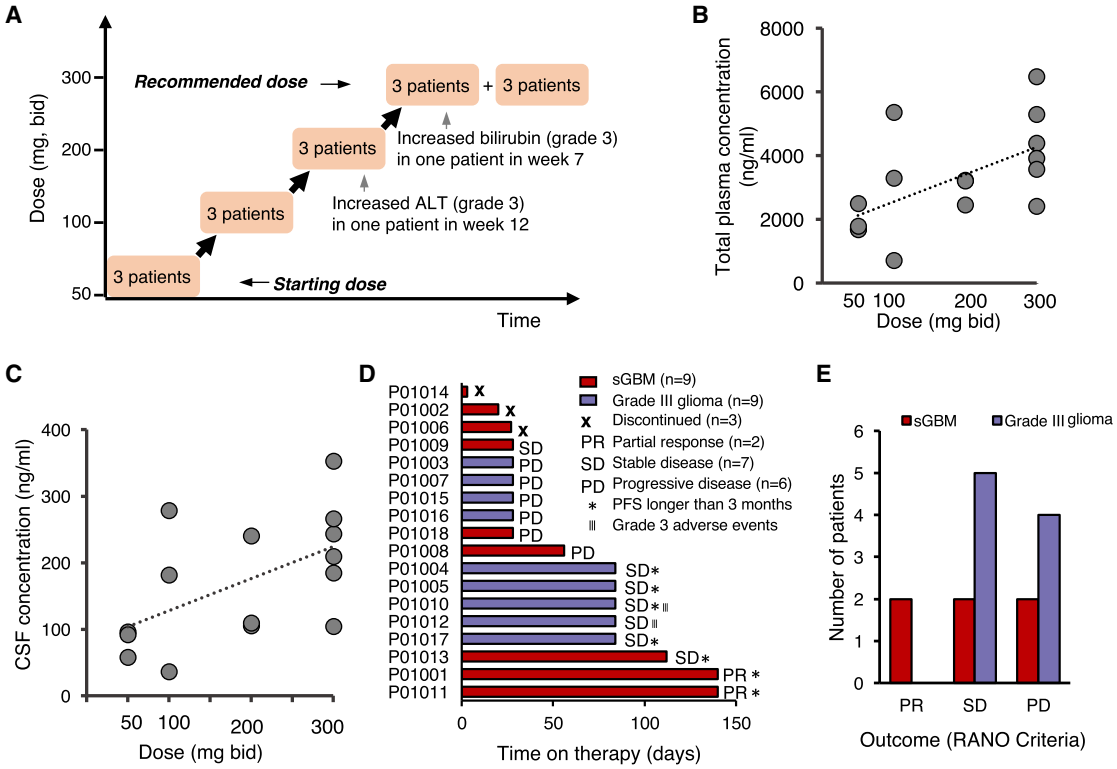

Figure 6. Safety and Efficacy of PLB-1001 in Human Patients

(A) The design of the Phase I 3+3 dose-escalation study of PLB-1001. The starting dose is 50 mg bid, and then increases to 100, 200, and 300 mg bid. At each dosage, a cohort of three patients are enrolled and the dose-limiting toxicities (DLT) are evaluated within the first 4 weeks of drug administration. No DLT in the enrolled patients are observed within the 4 weeks, but we observed 1 patient in the 200 mg dose cohort experienced increased ALT (grade 3) at week 12, while increased total bilirubin is observed in another patient in the 300 mg cohort at week 7. Considering the potential long-term toxicity and the pharmacokinetics data, the recommended phase II dose is 300 mg.

(B and C) Total plasma concentration (B) and CSF concentration (C) of PLB-1001 after single-dose treatment in patients. A linear trend of total plasma drug concentration versus drug dose was fitted and shown as the dashed line.

(D) The diagnosis, time on PLB-1001 therapy, and the response of the patients enrolled in the phase I clinical trial. The response was evaluated by the RANO criteria. The patients remained on therapy unless disease progression occurred.

(E) Clinical outcome of the phase I clinical trial in sGBM and grade III glioma patients.

See also Figures S4, S5, and S6 and Table S5.

at week 12 and increased total bilirubin in another patient treated with 300 mg bid dosage at week 7 (Figure 6D). These grade 3 AEs did not occur within the DLT observation period (4 weeks from the start of PLB-1001 treatment) and hence they were not considered as DLT. Common grade 1–2 AEs including increased serum lipase and glutamic oxalacetic transaminase and decreased albumin were observed. To evaluate the treatment outcome, the Response Assessment in Neuro-Oncology (RANO) criteria (Wen et al., 2017) has been used. Overall, out of the six sGBM patients who stayed in the trial, two achieved partial response (PR), two achieved stable disease (SD), and two had progressed disease (PD) (Figures 6D and 6E). Among the nine grade III glioma patients, five achieved SD and four had PD (Figures 6D and 6E; Table S5).

To determine the RP2D, pharmacokinetic test was performed and demonstrated that the plasma concentration in patients treated with 300 mg dosage had reached the corresponding 90% effective dose (ED90) in ZM-positive U87 cell line-derived xenograft models (Figure S6D; Table S6; STAR Methods). Taking into consideration the potential long-term toxicity effects, we recommend PLB-1001 monotherapy dosage as 300 mg bid.

The disease progression of the two sGBM patients who achieved PR was closely monitored by MRI scanning. Under PLB-1001 treatment, tumor shrinkage accompanied with symptom relief was observed in patients P01001 (Figure 7B) and P01011 (Figure S6E), and no radiological progression was detected in 16 weeks. However, at the 20th week of treatment, both patients showed non-measurable progression under RANO criteria (Wen et al., 2010), but symptom relief of the two patients continued. For P01001, the recurrent tumor was developed at the same location prior to the treatment and was resected and profiled by whole-genome and transcriptome sequencing. We then constructed the phylogenetic tree of this patient and found gained mutations in *PIK3CA*, *PIK3CG*, *PTEN*, *MSH2*, and deletions in *RB1* and *CIC* at recurrence after PLB-1001 treatment (Figure 7C). Single-sample gene set enrichment analysis (ssGSEA)

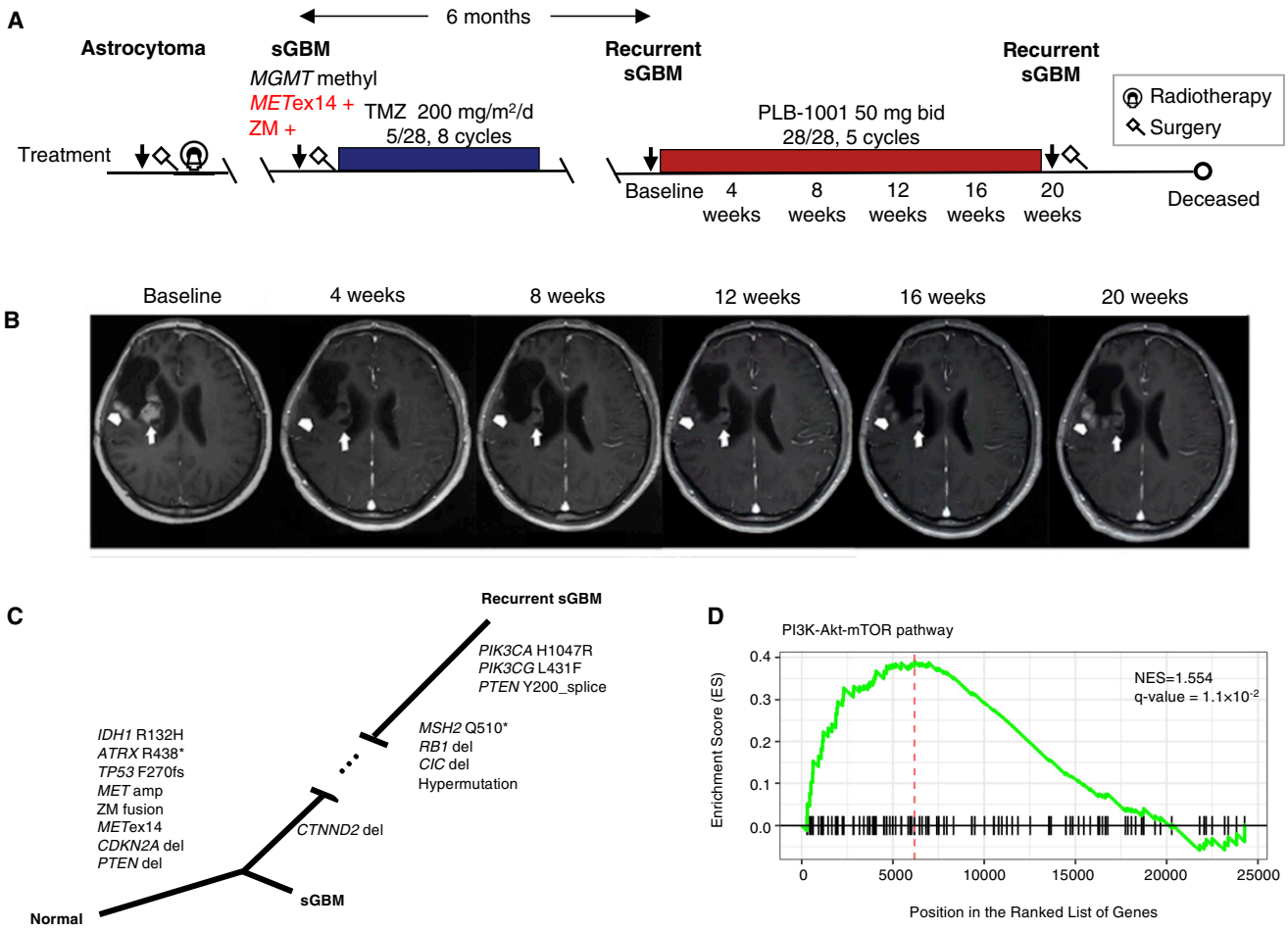

Figure 7. Case Study of a Patient Who Achieved Partial Response

(A) Diagram of the glioma progression and treatment in patient P01001. The patient was initially diagnosed of low-grade astrocytoma, which was resected and treated with radiotherapy. The tumor recurred locally and progressed into high-grade sGBM after 2 years and was surgically removed and treated by 6 cycles of temozolomide. As *MET*ex14 and ZM fusion was detected in this sGBM sample, the recurrent sGBM in the patient was later subscribed with 5 cycles of PLB-1001 treatment. At week 20 of treatment, the tumor recurred at the margin of resection area, and this recurrent sGBM was surgically removed and sequenced.

(B) The tumor (P01001) was monitored by MRI evaluation every 4 weeks (tumor site is marked by arrows). Tumor shrinkage was observed after 4 weeks of PLB-1001 treatment, and no radiological progression was detected until week 20 of treatment.

(C) The tumor evolution tree of P01001 was inferred from the whole genome and whole transcriptome sequencing of tumor samples from sGBM and the recurrent sGBM (rsGBM) after PLB-1001 treatment. Whole genome sequencing of the blood sample was used as normal control.

(D) Applying the single-sample gene set enrichment analysis (ssGSEA) on significantly upregulated genes in rsGBM versus sGBM. Elevated PI3K-Akt-mTOR pathway is detected at recurrence (NES = 1.554, q value = 1.1×10^{-2}).

analysis revealed elevated activity of PI3K-Akt-mTOR pathway in the recurrent tumor (Figure 7D), suggesting a potential mechanism of MET inhibitor resistance, which is in accordance with the observation that cell lines with both *MET*ex14 and *PIK3CA* mutation do not respond to MET inhibitor monotherapy (Liu et al., 2016).

In this phase I clinical trial, PLB-1001 monotherapy demonstrated a safety profile for sGBM or grade III glioma patients with ZM fusion and/or *MET*ex14. The median duration of response and PFS are 62.5 days and 80 days, respectively, and 7 out of 15 patients achieved PFS3. Recommended PLB-1001 monotherapy dosage is 300 mg bid.

DISCUSSION

By far, our study collected the largest cohort of sGBMs, combining cases from the AGGA and published datasets. The newly collected samples from East Asian population may reflect the difference between ethnic groups, which is an important factor in the implementation of precision medicine. We observed significantly higher rate of hypermutation in Caucasian than in Asian population, which may be contributed to by genetic background, environment factors, or the applied dose of TMZ.

In addition to previous reports of ZM fusion in glioma (Bao et al., 2014; Frampton et al., 2015), our study further identified

the enrichment of *MET*ex14 in sGBM and elucidated their roles in driving glioma progression. *MET*ex14 was also highly recurrent in lung cancer, and accelerated cell proliferation *in vitro* and in xenograft of small cell lung cancer cell lines (Kong-Beltran et al., 2006). Co-occurring of *MET*ex14 and ZM fusion is associated with enriched tumor-associated macrophages (TAM), which was reported to be associated with poor prognosis in glioma (Hambardzumyan et al., 2016; Shi et al., 2017). Co-occurrence of *TPR-MET* fusion and *MET*ex14 was reported to generate a chimeric protein with TPR dimerization domain and MET kinase domain, while excluding the JM domain (Cooper et al., 1984). Inclusion of exon 14 reduced the oncogenic potential of this fusion gene (Vigna et al., 1999), suggesting the role of *MET* exon 14 in regulating MET degradation. However, in the case of ZM fusion, the full-length transcript of ZM from patients show inclusion of the exon 14, suggesting mutations resulting in *MET*ex14 and ZM fusion occur on different copies of *MET* genes. Due to the scarcity of cases, further evidence is required to clarify the phasing of multiple *MET* alterations, as well as to explain the mechanism of the preference for co-occurring *MET* fusions with *MET*ex14 in various tumor types.

We described a small molecular inhibitor, PLB-1001, with high potency and specificity for the MET kinase domain. Structural modeling indicates that the additional interaction sites of PLB-1001 with MET kinase domain increase its binding affinity and specificity compared with crizotinib. Treatment of cell line and xenograft with *MET*ex14 or ZM fusion with PLB-1001 resulted in MET signaling inhibition and reduced tumor volume. Despite several ongoing MET-targeting clinical trials in glioma (Pearson and Regad, 2017), our study highlights a precision neuro-oncology approach by identifying patients with *MET* alterations. In our phase I clinical trial, PLB-1001 monotherapy demonstrated a safety profile for patients with ZM fusion and/or *MET*ex14. Moreover, 2/6 sGBM patients achieved PR, while SD was observed in 2/6 sGBM and 5/9 grade III glioma patients, indicating that PLB-1001 treatment is beneficial to not only sGBM but grade III glioma patients who harbored ZM and/or *MET*ex14. The lower response rate and short duration of response in patients may be contributed by the limited BBB penetration and intratumoral heterogeneity of gliomas. Nevertheless, our study provided an alternative therapeutic strategy for patients who have developed recurrent disease under TMZ-based standard therapy. Moreover, *MET* and ZM fusion are critical for chemoresistance in GBM (Huang et al., 2016; Zeng et al., 2017), and knock down of *MET* sensitizes tumor cell lines in response to TMZ treatment (Li et al., 2016). Given the lack of therapeutic options for recurrent tumor under TMZ treatment, our study has provided a promising therapeutic strategy of PLB-1001 mono- and combinatorial treatments with TMZ chemotherapy for patients with *MET* alterations.

STAR★METHODS

Detailed methods are provided in the online version of this paper and include the following:

- KEY RESOURCES TABLE
- CONTACT FOR REAGENT AND RESOURCE SHARING
- EXPERIMENTAL MODEL AND SUBJECT DETAILS
  - Human Patients and Samples
  - Rodent models
- METHOD DETAILS
  - Sample processing and sequencing
  - Validation of *MET*ex14 by Sanger sequencing
  - Validation of *PTPRZ1-MET* fusion by Sanger sequencing
  - Histology and immunohistochemical staining
  - Immunoblotting
  - Generation of lentiviral vectors encoding ZM fusion and transduction of lentiviral vector
  - Generation of adenoviral vectors encoding ZM fusions and transduction of adenoviral vectors
  - Cell viability assay
  - Analysis of drug sensitivity in patient-derived cells
  - Key information about PLB-1001
  - Target inhibition assay
  - Drug permeability assay
  - Detection of PLB-1001 concentration in rat brain
  - Subcutaneous xenografts and drug treatment
  - Intracranial xenograft implantation and tissue preparation
  - PLB-1001 treatment of intracranial xenograft mice model
  - Clinical trial of PLB-1001 treatment
- QUANTIFICATION AND STATISTICAL ANALYSIS
  - Mapping and mutation calling
  - Copy number alteration analysis
  - Hypermutation detection
  - Detection of gene fusions from RNA sequencing
  - Detection of *MET*ex14 from RNA sequencing
  - Definition of sGBM Specificity
  - Gene expression analysis and GSEA
  - Immune cell gene signatures
- DATA AND SOFTWARE AVAILABILITY
- ADDITIONAL RESOURCES

SUPPLEMENTAL INFORMATION

Supplemental Information includes six figures, six tables, and one data file and can be found with this article online at https://doi.org/10.1016/j.cell.2018.09.038.

ACKNOWLEDGMENTS

This work is a pilot study from the Chinese Glioma Genome Atlas (CGGA) and Asian Glioma Genome Atlas (AGGA) Research Networks. The authors would like to especially thank all contributors to CGGA and AGGA. The authors thank Dr. Fei Sun from HKUST for helpful comments and acknowledge TCGA research network, Gregory M. Kiez and Mehmet Kutman Foundation, and the Yale University Department of Neurosurgery for providing access to sequencing data. This work was supported by grants from National Key Research and Development Plan (2016YFC0902500); Natural Science Foundation of China (NSFC)/Research Grants Council (RGC), Hong Kong, China Joint Research Scheme (81761168038 to T.J. and N_HKUST606/17 to J.W.); National Natural Science Foundation of China (81502495, 81502606, and 81702460); Capital Foundation of Medical Developments (2016-1-1072); Beijing Municipal Administration of Hospitals Clinical Medicine Development of Special Funding Support (ZYLX201708); Beijing Nova Program (Z171100001117022); and Beijing Administration of Hospitals' Youth Program

(QML20160502). J.W. was also supported by Collaborative Research Fund (CRF), Hong Kong (C6002-17GF); Hong Kong Epigenomics Project (LKCCFL18SC01-E); and HKUST start-up and initiation grants and received substantial support from BDBI Lab. D.-H.N. was supported by the grant of Korea Health Technology R&D project through KHIDI funded by the Ministry of Health & Welfare, Republic of Korea (HI14C3418).

AUTHOR CONTRIBUTIONS

J.W. and T.J. conceptualized the project. J.W., H.H., Q.M., Z.B., Y.C., and T.J. interpreted the data. Z.B, Yanwei Liu, X.K., Yuqing Liu, and W.Z. undertook the prospective patient enrolment, diagnosis, and clinical follow-up. Q.M. and J.W. carried out the computational studies and discovered *MET*ex14 in glioma. H.H., J.C., Y.Z., F.Z., and F.W. performed experimental studies in cancer cell lines and xenografts. Z.B., K.W., Zheng Wang, C.Z., Z.Z., Z.Q., Zhiliang Wang, R.H., and Q.W. prepared patient samples for sequencing and partially performed data pre-processing. K.W., X.K., X.Q., W.L., and T.J. carried out the clinical trial of PLB-1001. Under the supervision of J.W., B.J. performed the hypermutation analysis; Y.C. and H.H. performed the study of glioma microenvironment; Y.N., J.K.S., H.-J.C., N.-G.H., and D.-H.N. performed data analysis of drug screening on patient-derived cells; and H.H., Q.M., Z.B., Y.C., and J.W. wrote the manuscript, which was further revised by J.K.S., D.-H.N., X.F., and T.J. All authors have read and approved the manuscript.

DECLARATION OF INTERESTS

All authors declare no competing interests.

Received: June 14, 2018
Revised: September 4, 2018
Accepted: September 18, 2018
Published: October 18, 2018

REFERENCES

Abate, F., Zairis, S., Ficarra, E., Acquaviva, A., Wiggins, C.H., Frattini, V., Lasorella, A., Iavarone, A., Inghirami, G., and Rabadan, R. (2014). Pegasus: a comprehensive annotation and prediction tool for detection of driver gene fusions in cancer. BMC Syst. Biol. *8*, 97.

Alexandrov, L.B., Nik-Zainal, S., Wedge, D.C., Aparicio, S.A.J.R., Behjati, S., Biankin, A.V., Bignell, G.R., Bolli, N., Borg, A., Børresen-Dale, A.-L., et al.; Australian Pancreatic Cancer Genome Initiative; ICGC Breast Cancer Consortium; ICGC MMML-Seq Consortium; ICGC PedBrain (2013). Signatures of mutational processes in human cancer. Nature *500*, 415–421.

Bai, H., Harmancı, A.S., Erson-Omay, E.Z., Li, J., Coşkun, S., Simon, M., Krischek, B., Özduman, K., Omay, S.B., Sorensen, E.A., et al. (2016). Integrated genomic characterization of IDH1-mutant glioma malignant progression. Nat. Genet. *48*, 59–66.

Bao, Z.-S., Chen, H.-M., Yang, M.-Y., Zhang, C.-B., Yu, K., Ye, W.-L., Hu, B.-Q., Yan, W., Zhang, W., Akers, J., et al. (2014). RNA-seq of 272 gliomas revealed a novel, recurrent *PTPRZ1-MET* fusion transcript in secondary glioblastomas. Genome Res. *24*, 1765–1773.

Bender, S., Gronych, J., Warnatz, H.-J., Hutter, B., Gröbner, S., Ryzhova, M., Pfaff, E., Hovestadt, V., Weinberg, F., Halbach, S., et al.; International Cancer Genome Consortium PedBrain Tumor Project (2016). Recurrent MET fusion genes represent a drug target in pediatric glioblastoma. Nat. Med. *22*, 1314–1320.

Brat, D.J., Verhaak, R.G., Aldape, K.D., Yung, W.K., Salama, S.R., Cooper, L.A., Rheinbay, E., Miller, C.R., Vitucci, M., Morozova, O., et al.; Cancer Genome Atlas Research Network (2015). Comprehensive, integrative genomic analysis of diffuse lower-grade gliomas. N. Engl. J. Med. *372*, 2481–2498.

Brennan, C.W., Verhaak, R.G.W., McKenna, A., Campos, B., Noushmehr, H., Salama, S.R., Zheng, S., Chakravarty, D., Sanborn, J.Z., Berman, S.H., et al.; TCGA Research Network (2013). The somatic genomic landscape of glioblastoma. Cell *155*, 462–477.

Ceccarelli, M., Barthel, F.P., Malta, T.M., Sabedot, T.S., Salama, S.R., Murray, B.A., Morozova, O., Newton, Y., Radenbaugh, A., Pagnotta, S.M., et al.; TCGA Research Network (2016). Molecular profiling reveals biologically discrete subsets and pathways of progression in diffuse glioma. Cell *164*, 550–563.

Cecchelli, R., Berezowski, V., Lundquist, S., Culot, M., Renftel, M., Dehouck, M.-P., and Fenart, L. (2007). Modelling of the blood-brain barrier in drug discovery and development. Nat. Rev. Drug Discov. *6*, 650–661.

Cooper, C.S., Park, M., Blair, D.G., Tainsky, M.A., Huebner, K., Croce, C.M., and Vande Woude, G.F. (1984). Molecular cloning of a new transforming gene from a chemically transformed human cell line. Nature *311*, 29–33.

Cui, J.J., Tran-Dubé, M., Shen, H., Nambu, M., Kung, P.-P., Pairish, M., Jia, L., Meng, J., Funk, L., Botrous, I., et al. (2011). Structure based drug design of crizotinib (PF-02341066), a potent and selective dual inhibitor of mesenchymal-epithelial transition factor (c-MET) kinase and anaplastic lymphoma kinase (ALK). J. Med. Chem. *54*, 6342–6363.

Dobin, A., Davis, C.A., Schlesinger, F., Drenkow, J., Zaleski, C., Jha, S., Batut, P., Chaisson, M., and Gingeras, T.R. (2013). STAR: ultrafast universal RNA-seq aligner. Bioinformatics *29*, 15–21.

Frampton, G.M., Ali, S.M., Rosenzweig, M., Chmielecki, J., Lu, X., Bauer, T.M., Akimov, M., Bufill, J.A., Lee, C., Jentz, D., et al. (2015). Activation of MET via diverse exon 14 splicing alterations occurs in multiple tumor types and confers clinical sensitivity to MET inhibitors. Cancer Discov. *5*, 850–859.

Gherardi, E., Birchmeier, W., Birchmeier, C., and Vande Woude, G. (2012). Targeting MET in cancer: rationale and progress. Nat. Rev. Cancer *12*, 89–103.

Hambardzumyan, D., Gutmann, D.H., and Kettenmann, H. (2016). The role of microglia and macrophages in glioma maintenance and progression. Nat. Neurosci. *19*, 20–27.

Huang, M., Liu, T., Ma, P., Mitteer, R.A., Jr., Zhang, Z., Kim, H.J., Yeo, E., Zhang, D., Cai, P., Li, C., et al. (2016). c-Met-mediated endothelial plasticity drives aberrant vascularization and chemoresistance in glioblastoma. J. Clin. Invest. *126*, 1801–1814.

Iyer, M.K., Chinnaiyan, A.M., and Maher, C.A. (2011). ChimeraScan: a tool for identifying chimeric transcription in sequencing data. Bioinformatics *27*, 2903–2904.

Johnson, B.E., Mazor, T., Hong, C., Barnes, M., Aihara, K., McLean, C.Y., Fouse, S.D., Yamamoto, S., Ueda, H., Tatsuno, K., et al. (2014). Mutational analysis reveals the origin and therapy-driven evolution of recurrent glioma. Science *343*, 189–193.

Kim, H., Zheng, S., Amini, S.S., Virk, S.M., Mikkelsen, T., Brat, D.J., Grimsby, J., Sougnez, C., Muller, F., Hu, J., et al. (2015a). Whole-genome and multisector exome sequencing of primary and post-treatment glioblastoma reveals patterns of tumor evolution. Genome Res. *25*, 316–327.

Kim, J., Lee, I.-H., Cho, H.J., Park, C.-K., Jung, Y.-S., Kim, Y., Nam, S.H., Kim, B.S., Johnson, M.D., Kong, D.-S., et al. (2015b). Spatiotemporal evolution of the primary glioblastoma genome. Cancer Cell *28*, 318–328.

Kong-Beltran, M., Seshagiri, S., Zha, J., Zhu, W., Bhawe, K., Mendoza, N., Holcomb, T., Pujara, K., Stinson, J., Fu, L., et al. (2006). Somatic mutations lead to an oncogenic deletion of met in lung cancer. Cancer Res. *66*, 283–289.

Lai, A.Z., Cory, S., Zhao, H., Gigoux, M., Monast, A., Guiot, M.-C., Huang, S., Tofigh, A., Thompson, C., Naujokas, M., et al. (2014). Dynamic reprogramming of signaling upon met inhibition reveals a mechanism of drug resistance in gastric cancer. Sci. Signal. *7*, ra38.

Lee, J.K., Wang, J., Sa, J.K., Ladewig, E., Lee, H.O., Lee, I.H., Kang, H.J., Rosenbloom, D.S., Camara, P.G., Liu, Z., et al. (2017). Spatiotemporal genomic architecture informs precision oncology in glioblastoma. Nat. Genet. *49*, 594–599.

Lee, J.K., Liu, Z., Sa, J.K., Shin, S., Wang, J., Bordyuh, M., Cho, H.J., Elliott, O., Chu, T., Choi, S.W., et al. (2018). Pharmacogenomic landscape of patient-derived tumor cells informs precision oncology therapy. Nat. Genet. *50*, 1399–1411.

Li, H. (2013). Aligning sequence reads, clone sequences and assembly contigs with BWA-MEM. arXiv:1303.3997.

Li, H., Handsaker, B., Wysoker, A., Fennell, T., Ruan, J., Homer, N., Marth, G., Abecasis, G., and Durbin, R.; 1000 Genome Project Data Processing Subgroup (2009). The Sequence Alignment/Map format and SAMtools. Bioinformatics *25*, 2078–2079.

Li, M.-Y., Yang, P., Liu, Y.-W., Zhang, C.-B., Wang, K.-Y., Wang, Y.-Y., Yao, K., Zhang, W., Qiu, X.-G., Li, W.-B., et al. (2016). Low c-Met expression levels are prognostic for and predict the benefits of temozolomide chemotherapy in malignant gliomas. Sci. Rep. *6*, 21141.

Liu, Y., Hu, H., Wang, K., Zhang, C., Wang, Y., Yao, K., Yang, P., Han, L., Kang, C., Zhang, W., and Jiang, T. (2014). Multidimensional analysis of gene expression reveals TGFB1I1-induced EMT contributes to malignant progression of astrocytomas. Oncotarget *5*, 12593–12606.

Liu, X., Jia, Y., Stoopler, M.B., Shen, Y., Cheng, H., Chen, J., Mansukhani, M., Koul, S., Halmos, B., and Borczuk, A.C. (2016). Next-generation sequencing of pulmonary sarcomatoid carcinoma reveals high frequency of actionable MET gene mutations. J. Clin. Oncol. *34*, 794–802.

Louis, D.N., Perry, A., Reifenberger, G., von Deimling, A., Figarella-Branger, D., Cavenee, W.K., Ohgaki, H., Wiestler, O.D., Kleihues, P., and Ellison, D.W. (2016). The 2016 World Health Organization Classification of Tumors of the Central Nervous System: a summary. Acta Neuropathol. *131*, 803–820.

Love, M.I., Huber, W., and Anders, S. (2014). Moderated estimation of fold change and dispersion for RNA-seq data with DESeq2. Genome Biol. *15*, 550.

Magi, A., Pippucci, T., and Sidore, C. (2017). XCAVATOR: accurate detection and genotyping of copy number variants from second and third generation whole-genome sequencing experiments. BMC Genomics *18*, 747.

Manning, G., Whyte, D.B., Martinez, R., Hunter, T., and Sudarsanam, S. (2002). The protein kinase complement of the human genome. Science *298*, 1912–1934.

Mazor, T., Pankov, A., Johnson, B.E., Hong, C., Hamilton, E.G., Bell, R.J.A., Smirnov, I.V., Reis, G.F., Phillips, J.J., Barnes, M.J., et al. (2015). DNA methylation and somatic mutations converge on the cell cycle and define similar evolutionary histories in brain tumors. Cancer Cell *28*, 307–317.

Mazor, T., Chesnelong, C., Pankov, A., Jalbert, L.E., Hong, C., Hayes, J., Smirnov, I.V., Marshall, R., Souza, C.F., Shen, Y., et al. (2017). Clonal expansion and epigenetic reprogramming following deletion or amplification of mutant *IDH1*. Proc. Natl. Acad. Sci. USA *114*, 10743–10748.

McLendon, R., Friedman, A., Bigner, D., Van Meir, E.G., Brat, D.J.M., Mastrogianakis, G., Olson, J.J., Mikkelsen, T., Lehman, N., Aldape, K., et al.; Cancer Genome Atlas Research Network (2008). Comprehensive genomic characterization defines human glioblastoma genes and core pathways. Nature *455*, 1061–1068.

Newman, A.M., Liu, C.L., Green, M.R., Gentles, A.J., Feng, W., Xu, Y., Hoang, C.D., Diehn, M., and Alizadeh, A.A. (2015). Robust enumeration of cell subsets from tissue expression profiles. Nat. Methods *12*, 453–457.

Nobusawa, S., Watanabe, T., Kleihues, P., and Ohgaki, H. (2009). IDH1 mutations as molecular signature and predictive factor of secondary glioblastomas. Clin. Cancer Res. *15*, 6002–6007.

Ohgaki, H., and Kleihues, P. (2013). The definition of primary and secondary glioblastoma. Clin. Cancer Res. *19*, 764–772.

Parsons, D.W., Jones, S., Zhang, X., Lin, J.C.-H., Leary, R.J., Angenendt, P., Mankoo, P., Carter, H., Siu, I.-M., Gallia, G.L., et al. (2008). An integrated genomic analysis of human glioblastoma multiforme. Science *321*, 1807–1812.

Pearson, J.R.D., and Regad, T. (2017). Targeting cellular pathways in glioblastoma multiforme. Signal Transduct. Target. Ther. *2*, 17040.

Robinson, J.T., Thorvaldsdóttir, H., Winckler, W., Guttman, M., Lander, E.S., Getz, G., and Mesirov, J.P. (2011). Integrative genomics viewer. Nat. Biotechnol. *29*, 24–26.

Sherry, S.T., Ward, M.H., Kholodov, M., Baker, J., Phan, L., Smigielski, E.M., and Sirotkin, K. (2001). dbSNP: the NCBI database of genetic variation. Nucleic Acids Res. *29*, 308–311.

Shi, Y., Ping, Y.-F., Zhou, W., He, Z.-C., Chen, C., Bian, B.-S.-J., Zhang, L., Chen, L., Lan, X., Zhang, X.-C., et al. (2017). Tumour-associated macrophages secrete pleiotrophin to promote PTPRZ1 signalling in glioblastoma stem cells for tumour growth. Nat. Commun. *8*, 15080.

Suzuki, H., Aoki, K., Chiba, K., Sato, Y., Shiozawa, Y., Shiraishi, Y., Shimamura, T., Niida, A., Motomura, K., Ohka, F., et al. (2015). Mutational landscape and clonal architecture in grade II and III gliomas. Nat. Genet. *47*, 458–468.

Trapnell, C., Williams, B.A., Pertea, G., Mortazavi, A., Kwan, G., van Baren, M.J., Salzberg, S.L., Wold, B.J., and Pachter, L. (2010). Transcript assembly and quantification by RNA-seq reveals unannotated transcripts and isoform switching during cell differentiation. Nat. Biotechnol. *28*, 511–515.

Vigna, E., Gramaglia, D., Longati, P., Bardelli, A., and Comoglio, P.M. (1999). Loss of the exon encoding the juxtamembrane domain is essential for the oncogenic activation of TPR-MET. Oncogene *18*, 4275–4281.

Wang, J., Cazzato, E., Ladewig, E., Frattini, V., Rosenbloom, D.I.S., Zairis, S., Abate, F., Liu, Z., Elliott, O., Shin, Y.J., et al. (2016). Clonal evolution of glioblastoma under therapy. Nat. Genet. *48*, 768–776.

Wen, P.Y., and Kesari, S. (2008). Malignant gliomas in adults. N. Engl. J. Med. *359*, 492–507.

Wen, P.Y., Macdonald, D.R., Reardon, D.A., Cloughesy, T.F., Sorensen, A.G., Galanis, E., Degroot, J., Wick, W., Gilbert, M.R., Lassman, A.B., et al. (2010). Updated response assessment criteria for high-grade gliomas: response assessment in neuro-oncology working group. J. Clin. Oncol. *28*, 1963–1972.

Wen, P.Y., Chang, S.M., Van den Bent, M.J., Vogelbaum, M.A., Macdonald, D.R., and Lee, E.Q. (2017). Response assessment in neuro-oncology clinical trials. J. Clin. Oncol. *35*, 2439–2449.

Yoshihara, K., Shahmoradgoli, M., Martínez, E., Vegesna, R., Kim, H., Torres-Garcia, W., Treviño, V., Shen, H., Laird, P.W., Levine, D.A., et al. (2013). Inferring tumour purity and stromal and immune cell admixture from expression data. Nat. Commun. *4*, 2612.

Zeng, A.-L., Yan, W., Liu, Y.-W., Wang, Z., Hu, Q., Nie, E., Zhou, X., Li, R., Wang, X.-F., Jiang, T., and You, Y.P. (2017). Tumour exosomes from cells harbouring PTPRZ1-MET fusion contribute to a malignant phenotype and temozolomide chemoresistance in glioblastoma. Oncogene *36*, 5369–5381.

Zhang, Y.-W., Wang, L.-M., Jove, R., and Vande Woude, G.F. (2002). Requirement of Stat3 signaling for HGF/SF-Met mediated tumorigenesis. Oncogene *21*, 217–226.

STAR★METHODS

KEY RESOURCES TABLE

REAGENT or RESOURCE	SOURCE	IDENTIFIER
Antibodies		
Phospho-Met (Tyr1234/1235) (D26) XP Rabbit mAb	CST	Cat# 3077; RRID: AB_2143884
Anti-Met (c-Met) (phospho Y1230 + Y1234 + Y1235) antibody	abcam	Cat# ab5662; RRID: AB_305029
Anti-Met (c-Met) (phospho Y1003) antibody	abcam	Cat # ab193270;
Anti-Met (c-Met) antibody	abcam	Cat# ab51067; RRID: AB_880695
Phospho-Stat3 (Tyr705) (D3A7) XP Rabbit mAb	CST	Cat# 9145; RRID: AB_2491009
Rabbit Anti-Stat3 Polyclonal Antibody	Santa Cruz	Cat# sc-7179; RRID: AB_661407
Phospho-Akt (Ser473) Rabbit mAb	CST	Cat# 4060; RRID: AB_2315049
Akt (pan) Rabbit mAb	CST	Cat# 4685; RRID: AB_2225340
Phospho-p44/42 MAPK (Erk1/2) Rabbit mAb	CST	Cat# 4370; RRID: AB_2315112
p44/42 MAPK (Erk1/2) Antibody	CST	Cat# 9102; RRID: AB_330744
Rabbit Anti-CD31 Monoclonal Antibody	ZSGB Bio	Cat# ZA-0568;
Rabbit Anti-Ki-67 Monoclonal Antibody	ZSGB Bio	Cat# ZA-0502;
Rabbit Anti-pHH3 Polyclonal Antibody	Manxin Bio	Cat# RAB-0693;
Phospho-cdc2 (Tyr15) Rabbit mAb	CST	Cat# 4539; RRID: AB_560955
Anti-β-Tubulin Mouse Monoclonal Antibody	CWBIO	Cat# CW0098M;
Anti-GAPDH Mouse Monoclonal Antibody	CWBIO	Cat# CW0100M;
Biological Samples		
Glioma tissues (Low-grade and GBM)	CGGA	N/A
Blood samples	CGGA	N/A
Chemicals, Peptides, and Recombinant Proteins		
pCDH-CMV-MCS-EF1α-Puro cDNA Cloning and Expression Lentivector	System Biosciences	Cat# CD510B-1
pPACKH1 Lentivector Packaging Kit	System Biosciences	Cat# LV500A-1
Astrocyte medium	ScienCell	Cat# 1801
CellTiter 96 AQueous One Solution Cell Proliferation Assay (MTS)	Promega	Cat# G3582
Critical Commercial Assays		
LANCE assay	Cerep	N/A
Deposited Data		
Raw sequencing data	Johnson et al., 2014	EGA: EGAS00001000579
Raw sequencing data	Kim et al., 2015a	EGA: EGAS00001001033
Raw sequencing data	Suzuki et al., 2015	EGA: EGAS00001001044
Raw sequencing data	Kim et al., 2015b	EGA: EGAS00001001041
Raw sequencing data	Wang et al., 2016	EGA: EGAS00001001800
Raw sequencing data	Wang et al., 2016	SRA: SRP074425
Raw sequencing data	Bao et al., 2014	GEO GSE48865
Raw sequencing data	This paper	EGA: EGAS00001003188
Crizotinib with MET tyrosine kinase domain	Cui et al., 2011	PDB: 2WGJ

(*Continued on next page*)

Continued

REAGENT or RESOURCE	SOURCE	IDENTIFIER
Human reference genome NCBI build 37, GRCh37	Genome Reference Consortium	http://hgdownload.cse.ucsc.edu/goldenPath/hg19/bigZips/
Human reference genome NCBI build 37 gencode annotation v19	The GENCODE Project	ftp://ftp.sanger.ac.uk/pub/gencode/Gencode_human/release_19/gencode.v19.annotation.gtf.gz
Experimental Models: Cell Lines		
U87 MG glioma cell line	Institute of Biochemistry and Cell Biology, Chinese Academy of Sciences	ATCC Number: HTB-14
Primary glioma cell N33	CGGA	N/A
Human astrocytes	ScienCell	Cat# 1800
Experimental Models: Organisms/Strains		
BALB/c nude mice	Charles River Laboratories	N/A
Sprague-Dawley rats	Charles River Laboratories	N/A
Oligonucleotides		
*MET*ex14 detection primer F	5′-AATCTTTTATTAGTGGTGGGAGCACAAT-3′	N/A
*MET*ex14 detection primer R	5′-GAATTAGGAAACTGATCTTTAATTTGC-3′	N/A
PTPRZ1-MET detection primer F	5′-CCGTCTGGAAATGCGAATCCTAAA-3′	N/A
PTPRZ1-MET detection primer R	5′-CAGGCCCAGTCTTGTACTCAGCAA-3′	N/A
Recombinant DNA		
pAAV-PTPRZ1-MET	This paper	N/A
Software and Algorithms		
BWA v0.7.15-r1140	Li, 2013	https://github.com/lh3/bwa
STAR v020201	Dobin et al., 2013	https://github.com/alexdobin/STAR
SAVI2	Wang et al., 2016	https://github.com/WangLabHKUST/SAVI
EXCAVATOR2 v1.1.2	Magi et al., 2017	https://sourceforge.net/projects/excavator2tool/
Chimerascan v0.4.5a	Iyer et al., 2011	https://code.google.com/archive/p/chimerascan/
Pegasus	Abate et al., 2014	https://github.com/RabadanLab/Pegasus
SAMtools v1.2	Li et al., 2009	http://samtools.sourceforge.net/
IGV v2.3.98	Robinson et al., 2011	http://software.broadinstitute.org/software/igv/
Cufflinks v2.2.1	Trapnell et al., 2010	http://cole-trapnell-lab.github.io/cufflinks/
DESeq2 v1.18.1	Love et al., 2014	https://bioconductor.org/packages/release/bioc/html/DESeq2.html
ESTIMATE v1.0.13	Yoshihara et al., 2013	http://bioinformatics.mdanderson.org/main/ESTIMATE:Overview
CIBERSORT v 1.06	Newman et al., 2015	https://cibersort.stanford.edu/

CONTACT FOR REAGENT AND RESOURCE SHARING

Further information and requests for resources and reagents should be directed to and will be fulfilled by the Lead Contact, Tao Jiang (taojiang1964@163.com).

EXPERIMENTAL MODEL AND SUBJECT DETAILS

All experiments were performed in accordance with the guidelines of the institution ethics committee (AAALAC standard). All analyses were approved by the ethic committees of the participating institutes (ethical committee of Beijing Tiantan Hospital, ethical committee of Sanbo Hospital, ethical committee of Tianjin Medical University General Hospital, ethical committee of The First Affiliated Hospital of Nanjing Medical University, ethical committee of Harbin Medical University, ethical committee of China Medical University, ethical committee of Samsung Medical Center) and were conducted in accordance with the principles expressed in the Declaration of Helsinki. Informed consent was obtained from all subjects before performing the experiments. For the model animals including mice and rats, all experiment operations were in accordance with instructions and permissions of the ethical committee of Beijing Tiantan Hospital. Due to small cohort size of the clinical trial, the influence of gender was not investigated in this study.

Human Patients and Samples

Sample acquisition

Glioma tissues, the corresponding genomic data and the patients' follow-up information (diagnosis, gender, age, WHO grade, and OS) were obtained from the Asian Glioma Genome Atlas (AGGA; including patients treated at Beijing Tiantan Hospital, Sanbo Hospital in Beijing, Tianjin Medical University General Hospital, The First Affiliated Hospital of Nanjing Medical University, Harbin Medical University, China Medical University, and Samsung Medical Center in Seoul). The biospecimens of the four patients from Samsung Medical Center were provided by Samsung Medical Center BioBank. The glioma tissues were snap-frozen in liquid nitrogen immediately after surgical resection and preserved in liquid nitrogen.

We also integrated sGBM samples from published datasets. The detailed information of these samples is described in Table S1.

Sample inclusion criteria

By definition, secondary glioblastoma (sGBM) in this study refers to glioblastoma that developed from low grade glioma (LGG). Therefore, all the samples included in this study must have clear record of LGG diagnosis. Most of the samples were accompanied with a blood specimen as normal control.

Surgically removed sGBM samples were obtained from newly diagnosed patients treated by the AGGA Group. Tumor histology of all patients was confirmed independently by two neuropathologists based on the 2016 edition of WHO classification of central nervous system tumors. All the patients in the study received similar treatments.

Rodent models

BALB/c nude mice

Female BALB/c nude mice (6-7 weeks old) were purchased from Charles River Laboratories. The mice were exposed to a 12-hour light/12-hour dark cycle, bred as specified-pathogen-free (SPF) and given food and water *ad libitum*. The mice were kept in the raising environment for a week before tumor cells transplantation. All procedures performed in this study were in accordance with instructions and permissions of the ethical committee of Beijing Tiantan Hospital. All mice were drug and test naive prior to initiating the experimental procedures performed and described in this paper.

Sprague-Dawley rats

Sprague-Dawley rats (12 males and 12 females) were purchased from Charles River Laboratories. The rats were 7-14 weeks old. The rats were bred in an SPF environment of 12-hour light/12-hour dark cycle and given food and water *ad libitum*. All experiment operations were in accordance with instructions and permissions of the ethical committee of Beijing Tiantan Hospital. All rats were drug and test naive.

Cell culture models

The human astrocytoma cell line U87 MG was obtained from the Institute of Biochemistry and Cell Biology, Chinese Academy of Sciences; the cells were cultured in Dulbecco's Modified Eagle's Medium (DMEM) supplemented with 10% FBS (HyClone), 100 units/ml penicillin and 100 μg/ml streptomycin (Invitrogen) at 37 °C in a humidified atmosphere of 5% CO_2. Human astrocytes (ScienCell) were cultured according to the manufacturer's protocol in astrocyte medium (ScienCell) containing 5% FBS, astrocyte growth supplement and 1% penicillin/streptomycin. N33 cell line was derived from fresh glioma bulk of a female patient immediately after operation in Beijing Tiantan Hospital. The patient-derived cell line N33 has been authenticated after it could be passaged stably. The short tandem repeat analysis showed that N33 has no cross-contamination of other human cell lines, and no 100% match with any cell line in ATCC data bank or DSMZ data bank.

METHOD DETAILS

Sample processing and sequencing

Genomic DNA from the tumor and the matched blood sample (where available) was extracted and confirmed for high integrity by 1% agarose gel electrophoresis. The DNA was subsequently fragmented, quality-controlled, and then pair-end libraries were prepared. For whole exome sequencing, Agilent SureSelect kit v5.4 was used for target capture. For targeted sequencing, a customized collection of 272 genes was captured using the Agilent SureSelectXT Custom kit. Sequencing was done on Illumina HiSeq 4000 platform using pair-end sequencing strategy. Samsung Medical Center (SMC) data was sequenced at SMC.

Total RNA from each tumor sample was extracted, and then depleted for tRNA and rRNA. After quality control and quantification, mRNA was reverse transcribed to cDNA, and then subjected to library preparation and sequencing.

Validation of *MET*ex14 by Sanger sequencing

RNA extraction and reverse transcription of the glioma specimens were performed as mentioned above. PCR was performed to detect *MET* exon 14 skipping. The primers sequences were as follows: forward 5′-AATCTTTTATTAGTGGTGGGAGCACAAT-3′; reverse 5′-GAATTAGGAAACTGATCTTTAATTTGC-3′. The reverse primer crosses exon 13 and exon 15 of *MET*. DNA polymerase (GoTaq, Promega) was used to amplify a 626-bp fragment with annealing temperature of 58°C. The product bands were extracted from agarose gel after electrophoresis and verified by Sanger sequencing.

Validation of *PTPRZ1-MET* fusion by Sanger sequencing

RNA of the glioma specimens was isolated using the RNAprep pure Tissue Kit (Tiangen Biotech) followed by cDNA synthesis (RevertAid RT Kit, Thermo Fisher Scientific) according to the manufacturers' instructions. Primers flanking the fusion points of *PTPRZ1-MET* (ZM) (forward: 5′-CCGTCTGGAAATGCGAATCCTAAA-3′ reverse: 5′-CAGGCCCAGTCTTGTACTCAGCAA-3′) were used to clone the sequences crossing the fusion points with DNA polymerase (GoTaq, Promega). The forward and the reverse primers were designed based on the *PTPRZ1* and *MET* segments that are common to all four fusion variants. Therefore, all four ZM fusion variants could be amplified using this pair of primers and amplifications of different sizes were produced (E1-E2: 337bp; E2-E2: 403bp; E3-E2: 583bp; E8-E2: 1207bp). The amplification product bands were extracted from agarose gel after electrophoresis and verified by Sanger sequencing. The sequencing reads were aligned to the known ZM fusion sequences to determine the presence and variant of ZM fusion in the given glioma specimen.

Histology and immunohistochemical staining

Glioma specimens were fixed in 4% paraformaldehyde for 24 h and stored in 70% ethanol until paraffin embedding. Embedded tissue was processed to 5 μm sections and stained with hematoxylin and eosin (HE). Based on the HE staining, the histopathological type and the glioma grade were determined according to the 2007 World Health Organization classification system.

Immunohistochemical staining of the relevant proteins was performed on 5 μm paraffin sections from glioma tissue. The sections were then deparaffinized, rehydrated and treated in 10 mM citrate buffer (100°C, 10 min) for antigen repair. Subsequently, the sections were immersed in ethanol containing 3% hydrogen peroxidase for 10 min to block endogenous peroxidase activity. The sections were incubated overnight at 4°C with the primary antibodies at the indicated concentration dilutions, followed by 3 × washing in phosphate-buffered saline and incubation with the secondary anti-rabbit or anti-mouse antibodies. The images were captured with Axio Imager 2 (Zeiss) after 3,3′-diaminobenzidine staining.

Immunoblotting

Tissue lysates or whole-cell lysates were prepared using RIPA buffer (Cell Signaling Technology). The protein concentration was detected by Coomassie Brilliant Blue using a micro plate spectrophotometer (Infinite M200 PRO, Tecan). Equal amounts of total protein (30 μg) from tissue or cell lysates were loaded on a 10% SDS/PAGE gel, transferred to a PVDF membrane (Merck Millipore), and detected using an ECL Western Blotting Detection System (Bio-Rad). Beta-Tubulin or glyceraldehyde 3-phosphate dehydrogenase (GAPDH) was used as the loading control. Goat anti-rabbit IgG-HRP or goat anti-mouse IgG-HRP were used as the secondary antibodies.

Generation of lentiviral vectors encoding ZM fusion and transduction of lentiviral vector

The coding sequence of the ZM fusion protein E2-E2 was cloned from glioma samples. The sequence was inserted into the lentiviral vector plasmid pCDH (System Biosciences). The pCDH plasmid carrying the fusion sequence was transduced into 293T cells with the lentiviral packaging plasmid mix (System Biosciences). The culture medium was collected once a day on two consecutive days and centrifuged with an ultracentrifuge at 25,000 rpm for 1.5 h. The precipitate was resuspended, aliquoted and stored at −80°C. This preparation was added to the U87 MG cell culture supplemented with 3 μg/ml polybrene (Sigma) in the medium. The medium was changed after 24 h. After 72 h, cells expressing the ZM fusion protein were selected during 3 days of treatment with puromycin. ZM fusion expression in the U87 MG cells was confirmed by RT-PCR.

Generation of adenoviral vectors encoding ZM fusions and transduction of adenoviral vectors

The human ZM E1-E2, ZM E2-E2 and *MET*ex14 coding sequences were amplified by PCR from cDNA derived from ZM-positive gliomas and cloned into a pShuttle-CMV vector. The sequences were then individually recombined into the pADxsi vector. Restriction enzyme digestion and sequencing were performed to confirm insertion of the right sequences. The recombinant plasmid was subsequently linearized by restriction enzyme digestion and transfected into HEK293A cells with Lipofectamine2000 (Thermo Fisher Scientific) for the generation of adenoviral vectors. The collected adenoviral vector was aliquoted and stored at −80°C before use. U87 MG cells, N33 or human astrocytes were separately treated in medium containing an appropriate titer of the adenoviral vector for 6h before medium change. ZM fusion and *MET*ex14 expression in each cell line was confirmed by RT- PCR.

Cell viability assay

The cells were seeded in 96-well plates at 800 cells per well in a total volume of 100 μl medium containing 10% FBS. During the following 6 days, cell viability was assessed everyday by MTS assay (CellTiter 96® AQueous One Solution Cell Proliferation Assay, Promega) according to the manufacturer's instructions.

Analysis of drug sensitivity in patient-derived cells

PDCs grown in serum-free medium were seeded in 384-well plates at a density of 500 cells per well in duplicate or triplicate for each drug treatment. PDCs were treated in a fourfold and seven-point serial dilution series from 4.88 nM to 20 μM. After 6 days of drug administration, cell viability was analyzed using ATP-monitoring system. Dose-response curve (DRC) fitting was performed using GraphPad Prism 5 and evaluated by measuring the Area Under the Curve (AUC) of the DRC. After normalization, best-fit lines were determined and AUC values were generated (Lee et al., 2018).

Key information about PLB-1001

PLB-1001 (C20H15F3N8) is also known as CBI-3103, IDD-100 or Bozitinib. The chemical structure can be described as follows: (6-(1-cyclopropyl-1H-pyrazol-4-yl)-3-[difluoro(6-fluoro-2-methyl-2H-indazol-5-yl)methyl]-[1, 2, 4]triazolo[4, 3-b]pyridazine).

This compound was initially developed by Crown Bioscience. Beijing Pearl Biotechnology, LLC has an exclusive right over this compound in China (patent number: ZL201210322359).

Target inhibition assay

Selective inhibition of MET kinase by PLB-1001 was validated in a LANCE kinase assay performed by Cerep incorporation (France). The efficiency of PLB-1001 in inhibiting 100 kinases including MET was tested through detection of the level of ULight/CREBtide-substrate phosphorylation after incubation with 2 μM of PLB-1001. Experimental conditions are indicated in Table S3.

Drug permeability assay

Drug permeability assay was performed by *in vitro* ADME Laboratory of Pharmaron. Inc (Beijing, China). P-glycoprotein (P-gp) transporter, encoded by *MDR1*, is an efflux pump on cerebral endothelial cells which blocks drug delivery to the CNS. We employed the widely received blood–brain barrier model MDCK (Madin-Darby Canine Kidney)-MDR1 cell line (Cecchelli et al., 2007) expressing P-glycoprotein (P-gp) to compare the permeability and the efflux effects of PLB-1001 and four other MET targeted drugs (Crizotinib, Temozolomide, Cabozantinib and Foretinib). MDCK-MDR1 cells were seeded in 96-well transwell to form a confluent monolayer. After 4-7 days of culture, the monolayer integrity was checked with TEER (Transepithelial Electrical Resistance) measurement. The drugs (PLB-1001, Crizotinib, Temozolomide, Cabozantinib or Foretinib) were added at a final concentration of 1 μM to the upper chamber of transwell (chamber A). After incubation (37°C, 2h), concentrations of the infiltrated drugs in the lower chamber (chamber B) were detected with LC-MS/MS. Using the same methods, the concentrations of the drugs infiltrated from chamber B to chamber A were also detected. Apparent permeabilities were calculated with the formula:

$$P_{app} = \frac{V_A}{Area \times time} \times \frac{[drug]_{acceptor}}{[drug]_{initial,donor}}$$

Area (area of a plate of 96-well transwell) = 0.143 cm^2; Time (incubation time) = 7200 s; V_A means volume of the accepter chamber. $V_{A(A\rightarrow B)}$ = 0.3 mL; $V_{A(B\rightarrow A)}$ = 0.1 mL. Efflux Rate was calculated with the formula:

$$Efflux\ Rate = \frac{P_{app(B\rightarrow A)}}{P_{app(A\rightarrow B)}}$$

Caco-2 cell monolayers model was employed to evaluate the potential of PLB-1001 to be the substrate of Breast Cancer Resistance Protein (BCRP). Cells were seeded in 96-well transwell to form a confluent monolayer. The upper chamber to lower chamber (A→B) and lower chamber to upper chamber (B→A) transport of PLB-1001 in HBSS (25 mM HEPES, pH 7.4) was measured across Caco-2 cell monolayers in the absence and presence of BCRP inhibitor, Novobiocin (30 μM). Incubations were performed at approximately 37°C, for 120 min, with functionality of the test system being confirmed using 10 μM Rosuvastatin as a positive control BCRP substrate. Transport of 1 μM PLB-1001 and control compounds were determined by quantifying substrate concentration with LC-MS/MS in the incubation medium of donor (lower) compartment at the beginning of the incubation period, and both donor (lower) and receiver (upper) compartments at the end of the incubation period. The data was used to calculate the apparent permeability (P_{app}). $P_{app(A\rightarrow B)}$ of PLB-1001 in the presence and absence of the BCRP inhibitor was compared, while $P_{app(B\rightarrow A)}$ of BCRP substrate Rosuvastatin in the presence and absence of the BCRP inhibitor was used as positive control. Calculation formula of P_{app} was as mentioned above.

Detection of PLB-1001 concentration in rat brain

Sprague-Dawley rats (12 males and 12 females, Charles River Laboratories) aged 7–14 weeks underwent 16 h of fasting before intra gastric administration of 4.5 mg/kg of PLB-1001. After administration, the rats were given food and water *ad libitum*. At 0.25 h, 3 h,

12 h and 24 h after administration, whole blood of 6 rats including 3 male and 3 female was collected into centrifuge tube with heparin anticoagulant. Plasma was obtained after centrifugation and stored at −80°C. The rats were immediately sacrificed after blood collection. Brain tissue was collected and washed in normal saline, dried with filter paper and homogenized in purified water at a ratio of 1:5 (g/ml). Following vortexing with methanol and centrifugation, the supernatant was collected and analyzed using liquid chromatography using Prominence30A (Shimadzu) coupled with tandem mass spectrometry to determine the PLB-1001 concentration. PLB-1001 concentration in plasma was analyzed using liquid chromatography after thaw.

Subcutaneous xenografts and drug treatment

U87 MG cells (1×10^6) transduced with a lentiviral vector expressing the ZM E2-E2 fusion or with a control vector were suspended in 100 μL PBS and injected subcutaneously into the flank of BALB/c nude mice (Charles River Laboratories). For experiments with MET inhibitors, mice carrying 100 mm^3 subcutaneous tumors were randomized to receive daily treatment with 50 mg/kg of Crizotinib or 10 mg/kg of PLB-1001 in 0.9% normal saline (injectable suspension) or an equal volume of normal saline by oral gavage. The tumor diameters were measured with a caliper, and the tumor volumes were estimated using the formula: $0.5 \times \text{length} \times \text{width}^2$. The mice were sacrificed when the tumors in the control group had reached the maximal size allowed by the Institutional Animal Care and Use Committee.

Intracranial xenograft implantation and tissue preparation

Female BALB/c nude mice (7-8 weeks) were implanted in the brain with U87 MG cells expressing the ZM E2-E2 fusion or control vector. Briefly, the mice were anesthetized with 0.25 mL of a cocktail of 10 mg/ml ketamine and 1 mg/ml xylazine, and the cells were implanted using cranial guide screws as previously described (Liu et al., 2014) (coordinates relative to bregma: 2.0 mm posterior, 2.0 mm lateral, 3.0 mm ventral). A Hamilton syringe and a micro infusion syringe pump (1μl/min; Harvard Apparatus) were used to implant 3×10^5 cells into the brain. The intracranial tumors were detected by MRI. Upon detection of obviously poor general conditions, the mice were sacrificed by intracardiac perfusion of PBS and 4% paraformaldehyde. The brains were extracted and fixed in 10% formalin for 24 h, embedded in paraffin, and sectioned into 5-μm slices.

PLB-1001 treatment of intracranial xenograft mice model

Female BALB/c nude mice were implanted in the brain with U87 MG cells expressing the ZM E2-E2 fusion (5×10^5 cells/ mouse) to form orthotopic tumors. The intracranial tumors were detected by MRI. Mice carrying intracranial tumors with a volume of 80 mm^3 were randomized to receive 50 mg/kg of PLB-1001 in 0.9% normal saline (injectable suspension) or an equal volume of normal saline by oral gavage. Upon detection of obviously poor general conditions, the mice were sacrificed by intracardiac perfusion of PBS and 4% paraformaldehyde. The brains were extracted for histology and immunohistochemistry analyses.

Clinical trial of PLB-1001 treatment

Study design and participants

We performed an open label, phase I, 3+3 dose-escalation study in Beijing (China; Table S5). The clinical trial was registered in National Clinical Trial (NCT02978261/ https://clinicaltrials.gov/ct2/show/NCT02978261) and approved by Medical Ethics Committee of Beijing Shijitan Hospital, Capital Medical University, Beijing, China. Eligible patients were over 18 years old, had pathologically confirmed recurrent high grade glioma, radiological progression after TMZ treatment with or without radiotherapy, a life expectancy of 3 months or more, RT-PCR followed by sanger sequencing validation of ZM expression, a Karnofsky Performance Scores (KPS) $\geq$ 50, measurable disease per the Response Assessment of Neuro Oncology (RANO) criteria guidelines (Wen et al., 2017) (including patients with recurrent tumor surgically removed), stable or decreasing dose of corticosteroids within 5 days, and adequate bone marrow (platelet count $\geq$ 75,000 per μL, absolute neutrophil count $\geq$ 1,500 per μL, and haemoglobin concentration $\geq$ 90 g/L), liver (total bilirubin concentrations, alanine aminotransferase and aspartate aminotransferase $\leq$ 1.5 times the upper limit of normal (ULN)), and renal function (i.e., serum creatinine, urea nitrogen $\leq$ 1.5 times ULN). Signed informed consent form was obtained from all patients. Exclusion criteria were previous or concurrent c-Met inhibitor or HGF-targeting therapy, presence of uncontrolled heart diseases, active peptic ulcer disease or gastritis, adverse events from prior anti-cancer therapy that have not resolved to Grade $\leq$ 1 (except for alopecia), major surgical procedures in the preceding 4 weeks, pregnant or nursing women and involved in other clinical trials within 30 days.

Procedures

PLB-1001 was provided by the sponsor (currently under development by Beijing Pearl Biotechnology, LLC) in the form of oral enteric capsule in 25 mg and 100 mg. We studied twice per day dosing of PLB-1001 with a modified Fibonacci dose-escalation design. The initially planned dose-escalation cohorts were 50 mg PLB-1001 twice per day, followed by 100 mg twice per day, followed by 200 mg twice per day, followed by 300 mg twice per day. If treatment was well tolerated (assessed weekly), patients continued treatment (at the planned level or frequency) until tumor progression reassessed by MRI or if patients were suspected to be unable to complete the trial. Patients were followed up weekly, MRI evaluation were performed monthly. All adverse events were monitored throughout the study period (until 28 days after participants' last PLB-1001 dose) and graded according to the National Cancer Institute's Common Terminology Criteria for Adverse Events (CTCAE; version 4.03). Dose-limiting toxicity was defined as a grade 3 adverse event that was attributable to study treatment within 28 days after PLB-1001 treatment. Resumption of treatment for patients with a

dose-limiting toxicity was permitted (when clinically appropriate) if the severity of the toxicity fell to grade I or lower and treatment was interrupted for no more than 2 weeks.

Full clinical histories were taken at screening. MRI evaluation were done at baseline and every 4 weeks after PLB-1001 therapy. MRIs were independently reviewed by an expert radiologist on the basis of RANO criteria. Partial Response (PR) requires all of the following: 50% decrease compared with baseline in the sum of products of perpendicular diameters of all measurable enhancing lesions sustained for at least 4 weeks; no new lesions; stable or reduced corticosteroid dose; and stable or improved clinically. Stable Disease (SD) defined by all of the following: does not qualify for complete response, partial response, or progression; and stable clinically. Progression Disease (PD) requires any of the following: 25% increase in sum of the products of perpendicular diameters of enhancing lesions; any new lesion; or clinical deterioration (Wen et al., 2010). If treatment discontinuation was anticipated before expected time, patients were encouraged to undergo MRI earlier. Laboratory tests for hematology, chemistry and urinalysis were done within the 14 days before the first dose of PLB-1001. Physical examinations and assessments of PFS performance status were done every 4 weeks. If progressive disease (PD) was observed after assessment by RANO criteria, patients dropped out from the trial.

Conversion from pharmacokinetics of PLB-1001 in xenografts transfected with ZM+ cell line to that of PLB-1001 in phase I clinical patients

To relate the PLB-1001 free plasma concentration to the potential drug efficacy, we applied PLB-1001 in xenografts transfected with ZM+ cell line. For each dose, *in vivo* inhibition rate of tumor volume (IR_{TV}) was calculated. For example, when 60% tumor volume was reduced comparing with that in control group, we defined the dosage as effective dose 60 (ED60); when 90% tumor volume was reduced, we defined the dosage as effective dose 90 (ED90). The total and free plasma concentration in mouse was estimated following linear regression equation based on pharmacokinetics: $Y = 1049.6X+1042$, where Y represents total plasma concentration and X represents drug dosage in mouse.

Outcomes

The primary endpoints were to establish the maximum tolerated dose of PLB-1001 as measured by dose-limiting toxicity and to define the recommended phase II dosage (RP2D). Secondary endpoints were to characterize pharmacokinetic/pharmacodynamics (PK/PD) profile of PLB-1001, to assess the PLB-1001 concentration in CSF and to define the preliminary objective response according to the RANO criteria.

Statistical analysis

Analysis of tolerability and toxicity was based on all patients in each dosing cohort who received at least one cycle (28 days) of one dose of the study drug. The maximum tolerated dose was based on the dose-limiting toxicities noted during PLB-1001 treatment. We used descriptive statistics to summarize AE data. We summarized response analysis that was done in patients who underwent a baseline assessment and at least one scheduled post-baseline tumor assessment by MRI. We collected CSF concentration of PLB-1001 in all patients for comparison analysis with parameters of plasma pharmacokinetics. All statistical tests were two-sided and assumed a two-sided significance level of 0.05.

QUANTIFICATION AND STATISTICAL ANALYSIS

Mapping and mutation calling

Valid DNA sequencing data were mapped to the reference human genome (UCSC hg19) using Burrows-Wheeler Aligner (bwa mem) with default parameters. Then, SAMtools and Picard (Broad Institute) were used to sort the reads by coordinates and mark duplicates (mark duplication was not done for deep sequencing). Statistics such as sequencing depth and coverage were calculated based on the resultant BAM files.

SAVI2 was used to identify somatic mutations (including single nucleotide variations and short insertion/deletions) as previously described. In this pipeline, SAMtools mpileup and bcftools were used to perform variant calling, then the preliminary variant list was filtered to remove positions with no sufficient sequencing depth, positions with only low-quality reads, and positions that are biased toward either strand. Somatic mutations were identified and evaluated by an Empirical Bayesian method. In particular, mutations with the mutation allele frequency in tumors significantly higher than that in normal control were selected (Wang et al., 2016). The reported mutations were further selected based on known driver genes of LGG and glioblastoma (Wang et al., 2016).

Copy number alteration analysis

For WES and target sequencing data, Excavator2 was used to estimate CNA (copy number alteration) status of the known driver genes of glioma, including *CIC*, *FUBP1*, *CDKN2A*, *CDK4*, *MDM2*, *MET, EGFR, PTEN, PDGFRA* and *TP53*. The window size was selected as 10,000, and all other parameters were as default.

XCAVATOR, which uses the same algorithm as EXCAVATOR2, was used to analyze CNA in whole genome sequencing data. Window size was set to be 10000, and other default parameters were used.

Hypermutation detection

Hypermutated samples were detected using an in-house software based on a scaled mutation load (ML) per sample and a hypermutation score (HM) (Wang et al., 2016). For the samples without matched normal sample sequenced, we filtered out the SNPs

recorded in the dbSNP database (Sherry et al., 2001). For identification of mutations using RNA-sequencing data, we did not consider the mutations located in splicing sites. After filtering of significant mutations, we considered the number of significant mutations as the mutation load for targeted-sequencing and RNA-sequencing data, and the mutation load for whole-exome sequencing data is the number of significant mutations divided by 10. The hypermutation score (HM Score) was defined based on our previous study (Wang et al., 2016) and the TMZ-treatment-related signature (Signature 11) (Alexandrov et al., 2013) as

$$HM = \frac{f_{C\to T}(N)}{ML} + \frac{f_{C\to T}(C)}{f_{C\to T}(N)} + \frac{sign(f_{C\to T}(C) - f_{C\to T}(T))f_{C\to T}(T)}{f_{C\to T}(N)}$$

where the function $f_{C->T}(x)$ is the number of mutations from cytosine C to thymine T followed by a nucleotide x along the 3-prime direction in the reference genome, and the function sign(y) = 1 if y > = 0, and −1 otherwise. The letter N denotes any bases A, T, G or C. The three terms in the HM score are designed to capture the three features of hypermutated samples due to TMZ treatment: (1) the dominant mutation type is C- > T, (2) those C- > T mutations are primarily followed by a nucleotide C, and (3) T is the second most succeeding nucleotide of the C- > T mutated sites. The in-house software will be available under request.

Detection of gene fusions from RNA sequencing

Chimerascan (Iyer et al., 2011) was used to produce a gene fusion candidates from RNA sequencing data and then further annotated with Pegasus (Abate et al., 2014). The fusions were selected by: (i) Pegasus score > 0.5; (ii) either more than 400 spanning reads or at least 2 split reads supporting fusion; and (iii) the two fusion partners being separated from each other by at least 50 kb.

Detection of *MET*ex14 from RNA sequencing

We detected *MET* exon 14 skipping based on spanning reads over the junction of exon 13 and exon 15. Briefly, RNA sequencing reads were aligned to the reference genome (hg19) using STAR, and then the reads containing a jump of 3226 bp from chr7:116411700 were counted. The spanning reads were manually checked in Integrative Genomic Viewer to remove false positives such as PCR artifacts and potential mapping errors. Sashimi plot was used to visualize the skipping reads.

Definition of sGBM Specificity

To measure the specificity of an alteration in sGBM compared with LGG and pGBM, the fold change was calculated using the following formula:

$$sGBM\ specificity = \frac{s \times (P + L)}{S \times (p + l)}$$

where s, p, l represent the number of altered sGBM, pGBM, LGG patients respectively, while S, P, L stand for that of total sGBM, pGBM and LGG cases.

Gene expression analysis and GSEA

The human reference genome hg19, and genome annotation file were downloaded from UCSC genome browser. The clean RNA sequencing reads were mapped to the reference genome using STAR. Gene expression, in FPKM, was calculated by Cufflinks. Differentially expressed genes were selected based on fold change and adjusted P value which was calculated by DESeq2. GSEA was used for gene set enrichment analysis. Normalized enrichment scores (NES) were calculated for gene sets which were downloaded from MSigDB database version 6.1 (http://software.broadinstitute.org/gsea/msigdb).

Immune cell gene signatures

Gene expression level, represented as FPKM, was processed by Cibersort (Newman et al., 2015) under absolute mode. The resultant absolute immune fraction scores of 22 immune cell types between different groups were compared using Wilcoxon rank-sum test.

DATA AND SOFTWARE AVAILABILITY

The accession numbers for sequencing data reported in this paper are EGAS00001003188, EGAS00001000579, EGAS00001001033, EGAS00001001044, EGAS00001001041, EGAS00001001800; SRA: SRP074425; GEO: GSE48865.

ADDITIONAL RESOURCES

This study involves an open label, phase I, 3+3 dose-escalation study in Beijing (China; Table S5). The clinical trial was registered in National Clinical Trial (NCT02978261/https://clinicaltrials.gov/ct2/show/NCT02978261) and approved by Medical Ethics Committee of Beijing Shijitan Hospital, Capital Medical University, Beijing, China.

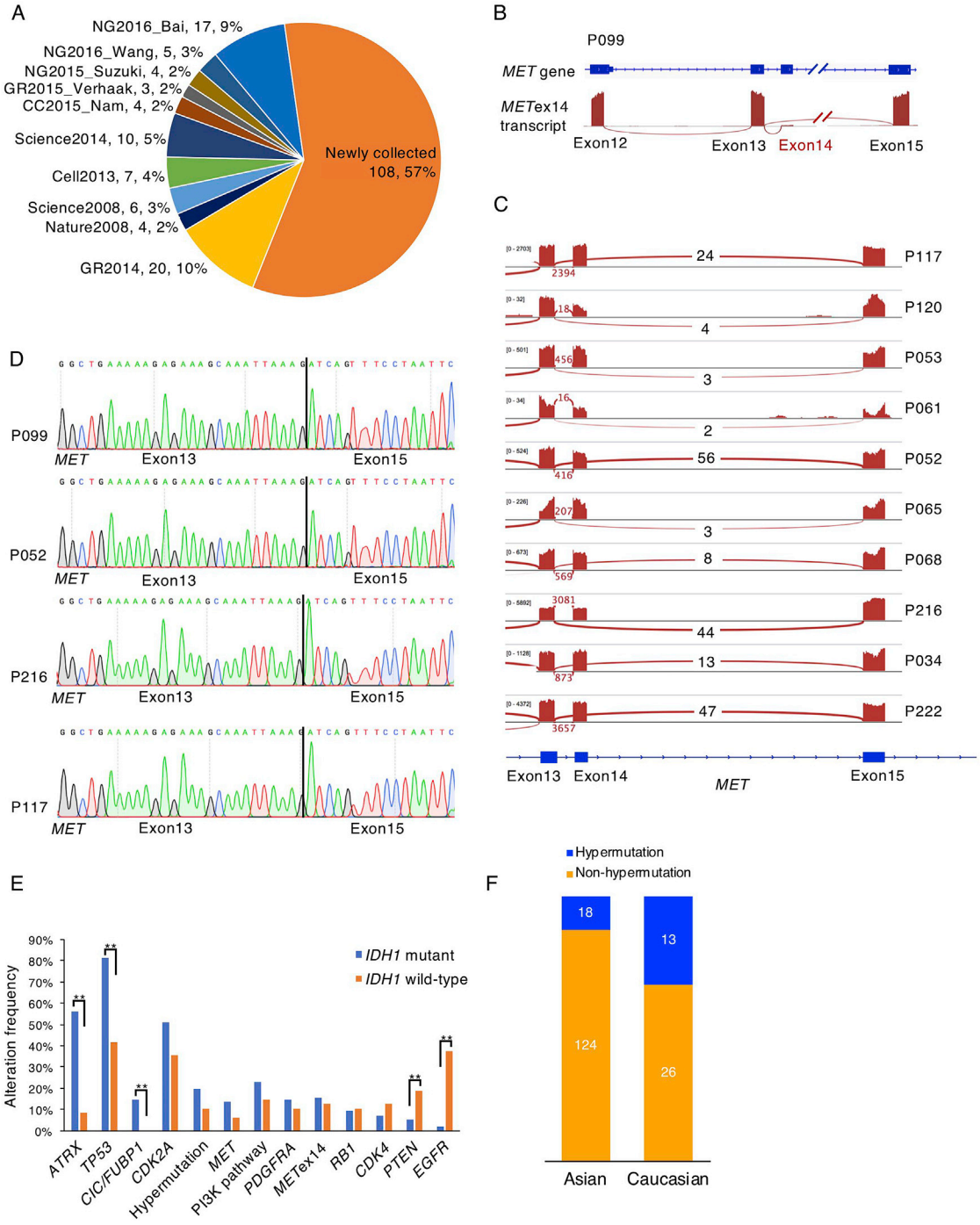

Figure S1. Comparison of Pairwise Correlations, Mutation Frequencies, and Survival in sGBM Patients, Related to Figure 1

(A) 188 sGBM samples were analyzed, among them 108 are newly collected from AGGA, and 80 were retrieved from published datasets.

(B) Sashimi plot of RNA-seq data from a *MET*ex14-positive sGBM (P099), showing a large number of reads spanning *MET* exon 13 and exon 15 junction.

(C) Sashimi plot of RNA-seq data from all *MET*ex14-positive sGBM patients, with the number of exon 14-skipping reads shown.

(D) *MET*ex14 is validated by cDNA amplification and Sanger sequencing of in sGBM P099, P052, P216 and P117, respectively.

(E) Comparison of mutation frequency in sGBM patients that are *IDH* mutant and *IDH* wild-type.

(F) Fractions of hypermutated glioma samples observed in Caucasian population and Asian population. Gliomas with hypermutation (HM) were colored blue, and non-hypermutated (non-HM) patients are colored orange. HM status was not available for 7/188 samples.

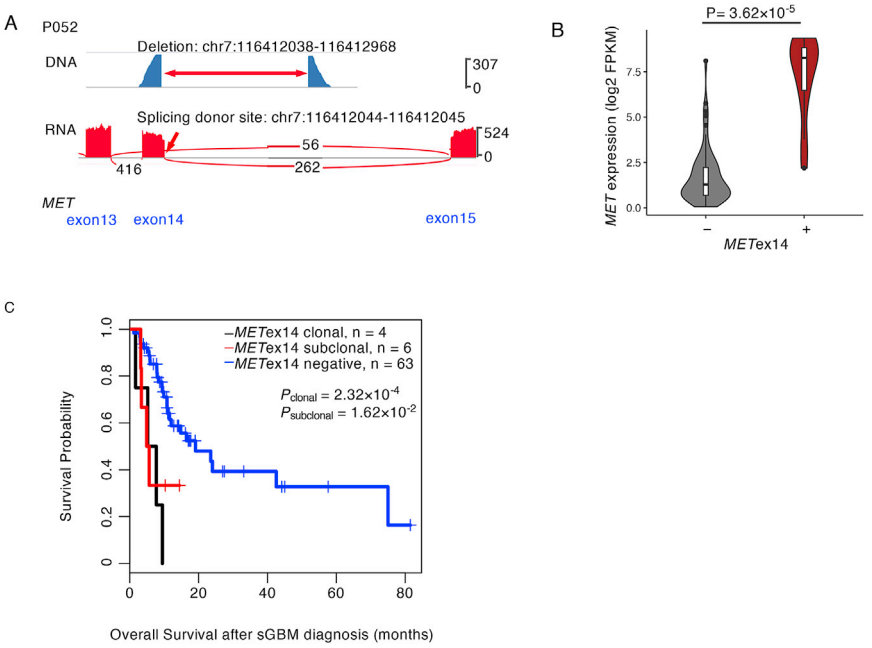

Figure S2. *MET* Exon 14 Skipping Is Caused by Mutations and Is Associated with *MET* Overexpression and Poor Prognosis in sGBM, Related to Figure 2

(A) Deletion of chr7:116412038-116412968 was detected in the genomic DNA of sGBM patient P052, resulting in the removal of the splicing donor site of the *MET* exon 14 (chr7:116412044-116412045) and thus causing exon 14 skipping on *MET* transcripts.

(B) Expression levels of *MET* in sGBM with *MET*ex14 and in *MET*ex14-negative samples.

(C) Overall survival of sGBM patients with subclonal (reads supporting *MET*ex14 were between 2 and 10), clonal *MET*ex14 (reads supporting *MET*ex14 were more than 10) and sGBM without *MET*ex14 alteration.

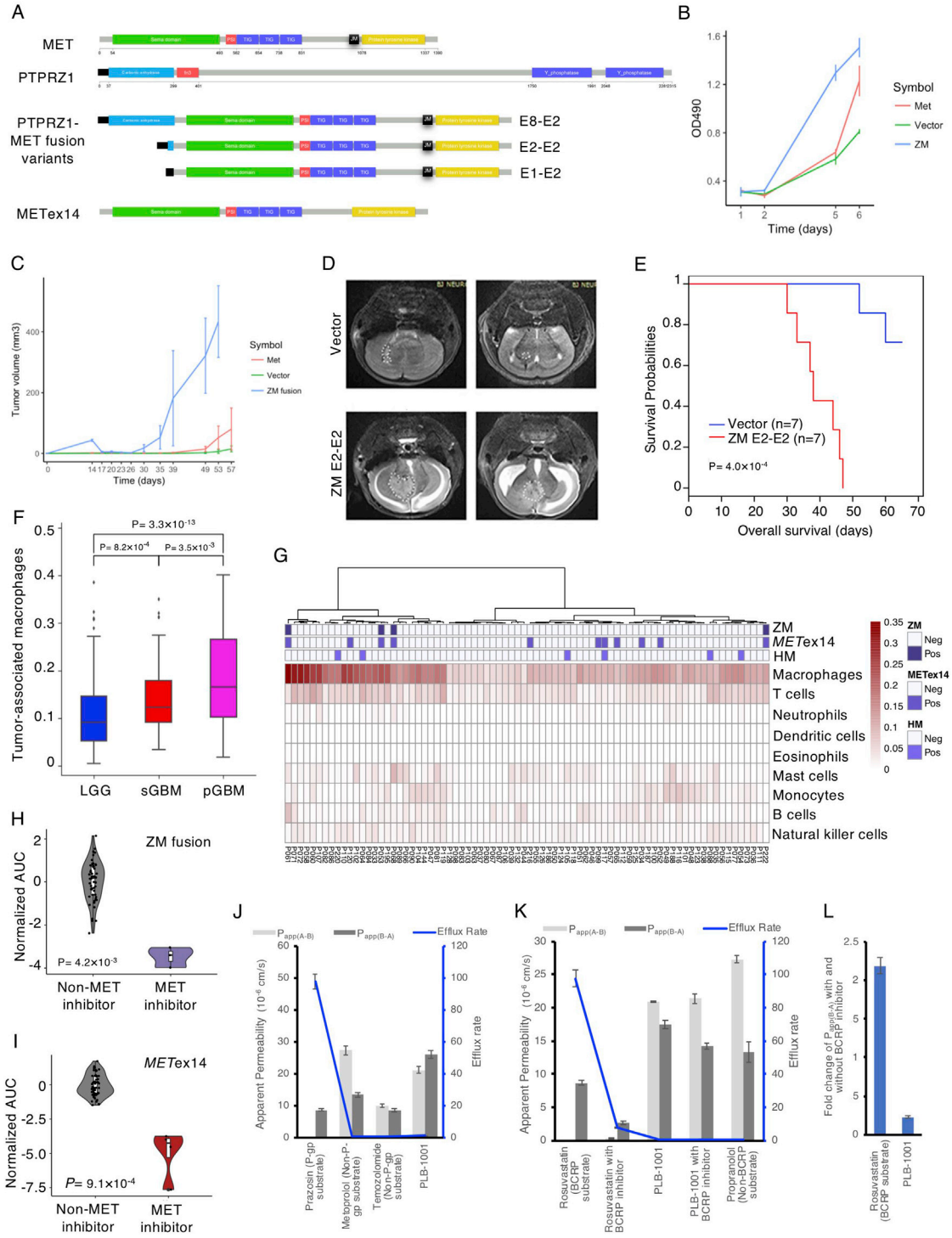

Figure S3. *MET* Alterations Promote Tumor Growth in Xenograft Model, Related to Figures 3 and 4

(A) Protein domains of the predicted translation product of wild-type *MET*, *PTPRZ1*, ZM fusion (E8-E2, E2-E2 and E1-E2 fusion variants are shown, respectively) and *MET*ex14.

(B) Growth curve of U87 MG cells stably expressing ZM fusion (E2-E2) following lentiviral vector transduction or *MET* overexpression. The mean ± SD of OD_{490} values derived from two experiments with 6 replicates for each indicated cell type is shown.

(C) Growth curves of subcutaneous tumors formed by U87 MG cells transduced by lentiviral vector encoding the ZM fusion (E2-E2) (n = 7) or *MET* (n = 7), or by the control vector (n = 7). Data are presented as means ± SD

(legend continued on next page)

(D) Representative MRI images of intracranial tumors formed by U87 MG cells stably expressing ZM fusion (E2-E2) or control vector at 30 days post transplantation.

(E) Kaplan-Meier survival curves of the mice carrying intracranial tumors formed by U87 MG cells stably expressing ZM fusion (E2-E2) or control vector. A Hamilton syringe and a micro infusion syringe pump (1 μl/min; Harvard Apparatus) were used to implant 3×10^5 cells into the brain.

(F) Comparison of abundance of macrophage populations in LGG (n = 202), sGBM (n = 65), and pGBM (n = 120), by *in silico* deconvolution using CIBERSORT. The p value is calculated by Wilcoxon rank-sum test.

(G) Heatmap illustrating the abundance of immune cell types in the sGBM microenvironment, by *in silico* deconvolution using CIBERSORT.

(H and I) A patient-derived cell line harboring ZM fusion (H) and a patient-derived *MET*ex14-positive cell line (I) demonstrate significantly lower normalized AUC ($p = 4.0 \times 10^{-3}$ and 9.0×10^{-4}, respectively, by rank-sum test) in response to four MET inhibitors compared to a group of receptor tyrosine kinases. The AUC was calculated from the dose-response curve in a fourfold and seven-point serial dilution series from 4.88 nM to 20 μM of 60 drugs (four MET inhibitors and fifty-six non-MET inhibitors).

(J) Comparison of the apparent permeability (left axis represented by the bar plot) and efflux rate (right axis represented by the blue line) of P-glycoprotein (P-gp) substrate Prazosin, non-P-gp substrates (Metoprolol and Temozolomide) and PLB-1001 in MDCK-MDR1 cell permeability assay.

(K) Caco-2 cell permeability assay demonstrates the permeability (left axis represented by the bar plot) and efflux rate (right axis represented by the blue line) of Rosuvastatin (BCRP substrate), PLB-1001 and Propranolol (non-BCRP substrate) in the presence and absence of BCRP inhibitor.

(L) Fold change of apparent permeability from lower chamber to upper chamber ($P_{app}B \rightarrow A$) of Rosuvastatin (BCRP substrate) and PLB-1001 in the absence versus presence of BCRP inhibitors in Caco-2 cell permeability assay.

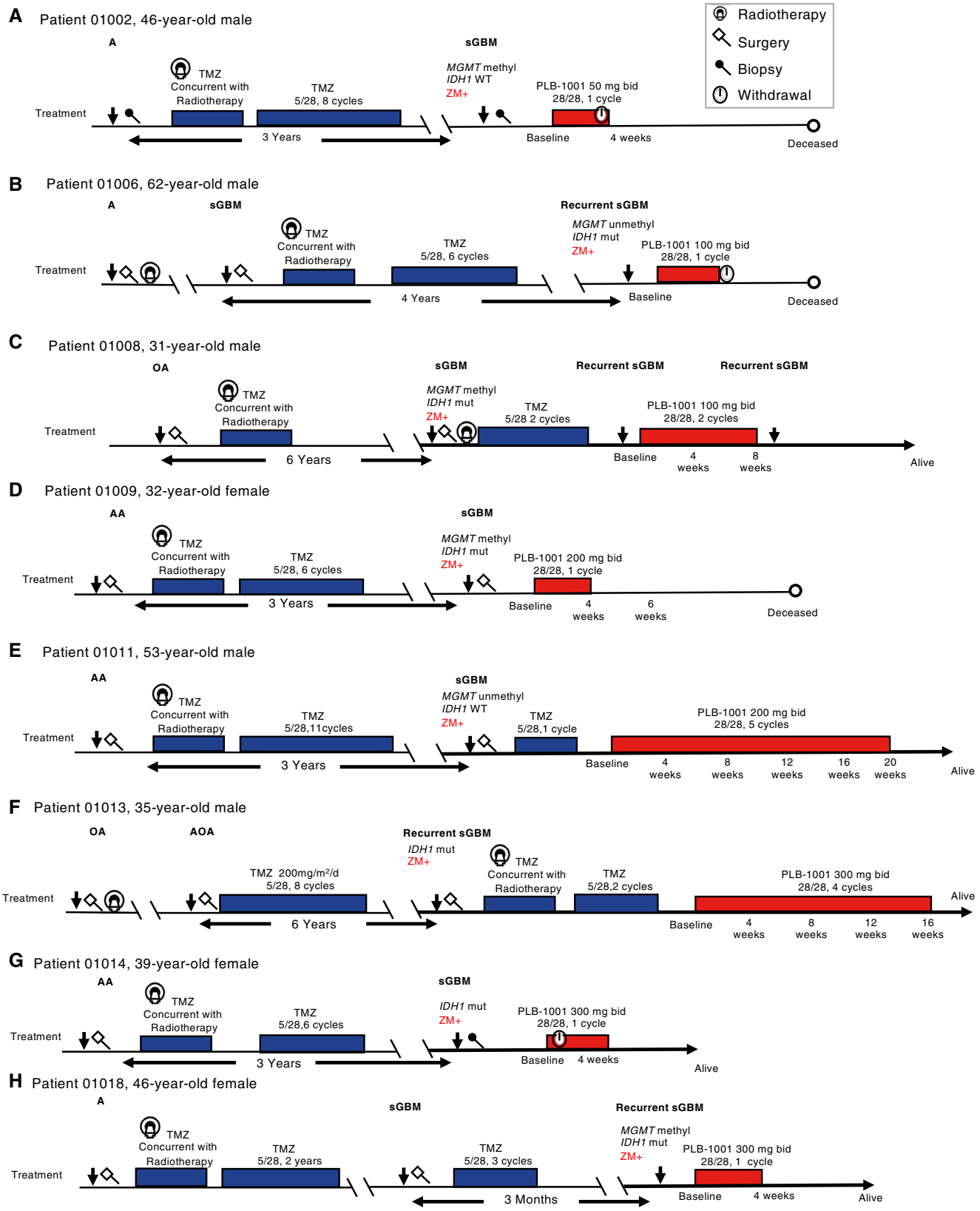

(legend on next page)

Figure S4. Clinical Records of sGBM Patients Enrolled in PLB-1001 Trial, Related to Figure 6

(A) Diagram of the glioma progression and treatment in patient P01002. Patient P01002 was a 46-year-old male, diagnosed with sGBM after 3 years since the initial astrocytoma (A) was resected and treated with TMZ concurrent with radiotherapy and followed by 8 cycles of TMZ treatment. ZM fusion was detected in the sGBM sample, and the patient was later subscribed with PLB-1001 treatment (50 mg bid). The patient withdrew from the clinical trial because of the drug-unrelated tumor stroke. Fortunately, the patient is still alive with a 591-day PPS.

(B) Diagram of the glioma progression and treatment in patient P01006. Patient P01006 was a 64-year-old male. After 15 years since the initial low-grade A was resected and treated with radiotherapy, the tumor recurred locally and progressed into sGBM. Despite treated with TMZ concurrent with radiotherapy followed by 6 cycles of TMZ, the sGBM recurred. ZM fusion was detected in the recurrent sGBM sample, and the patient was later subscribed with PLB-1001 treatment (100 mg bid). However, the patient withdrew from the clinical trial because of the drug-unrelated pneumonia. The patient died with a 75-day PPS.

(C) Diagram of the glioma progression and treatment in patient P01008. Patient P01008 was a 31-year-old male. After two years since the initial low-grade oligodendro-astrocytoma (OA) was resected and treated with TMZ concurrent with radiotherapy, the tumor recurred locally and progressed into sGBM. The sGBM was surgically removed and treated with 2 cycles of temozolomide following radiotherapy. ZM fusion was detected in the sGBM sample, and the patient was later subscribed with PLB-1001 treatment (100 mg bid) after the failure of TMZ treatment. MRI evaluation after 4 and 8 weeks of PLB-1001 treatment however demonstrated tumor progression accompanied by stable symptom. Fortunately, the patient is still alive with a 349-day PPS.

(D) Diagram of the glioma progression and treatment in patient P01009. Patient P01009 was a 32-year-old female diagnosed with sGBM after 3 years since the initial anaplastic astrocytoma (AA) was resected and treated with TMZ concurrent with radiotherapy and followed by 6 cycles of TMZ subsequently. ZM fusion was detected in the sGBM sample, and the patient was later subscribed with PLB-1001 treatment (200 mg bid). MRI evaluation after 4 and 6 weeks of PLB-1001 treatment demonstrated stable tumor volume accompanied by worse symptom. The patient died with a 194-day PPS.

(E) Diagram of the glioma progression and treatment in patient P01011. Patient P01011 was a 53-year-old male diagnosed with sGBM after 3 years since the initial AA was resected and treated with TMZ concurrent with radiotherapy followed by 11 cycles of TMZ. ZM fusion was detected in the sGBM sample, and the patient was later subscribed with PLB-1001 treatment (200 mg bid). MRI evaluation after 16 weeks of PLB-1001 treatment demonstrated tumor shrinkage accompanied by symptom relief. No radiological progression was detected until 20 weeks after PLB-1001. The patient is still alive with a 265-day PPS.

(F) Diagram of the glioma progression and treatment in patient P01013. Patient P01013 was a 35-year-old male with sGBM after treatment with 8 cycles of temozolomide. Since the initial low-grade OA was treated with radiotherapy, the tumor recurred locally and progressed into anaplastic oligodendroastrocytoma (AOA). After 6 years, the tumor progressed into sGBM. ZM fusion was detected in the sGBM sample, and the patient was later subscribed with TMZ concurrent with radiotherapy followed by 2 cycles of TMZ, and finally the PLB-1001 treatment (300 mg bid). MRI evaluation after 16 weeks of PLB-1001 treatment demonstrated stable tumor volume accompanied by symptom relief. The patient still alive with a 337-day PPS.

(G) Diagram of the glioma progression and treatment in patient P01014. Patient P01014 was a 39-year-old female, diagnosed with sGBM after 3 years since the initial AA was resected and treated with TMZ concurrent with radiotherapy followed by 6 cycles of TMZ subsequently. ZM fusion was detected in the sGBM sample, and the patient was later subscribed with PLB-1001 treatment (300 mg bid). However, the patient withdrew from the clinical trial because of the drug-unrelated dysphagia. The patient is still alive with a 202-day PPS.

(H) Diagram of the glioma progression and treatment in patient P01018. Patient P01018 was a 46-year-old male treated after 3 cycles of TMZ. After 2 years since the initial low-grade A was resected and treated with TMZ concurrent with radiotherapy followed by 2 years of TMZ treatment, subsequently, the tumor recurred locally and progressed into sGBM. ZM fusion was detected in the recurrent sGBM sample, and the patient was later subscribed with PLB-1001 treatment (300 mg bid). MRI evaluation after 4 weeks of PLB-1001 treatment demonstrated increased tumor volume. The patient is still alive with a 96-day PPS.

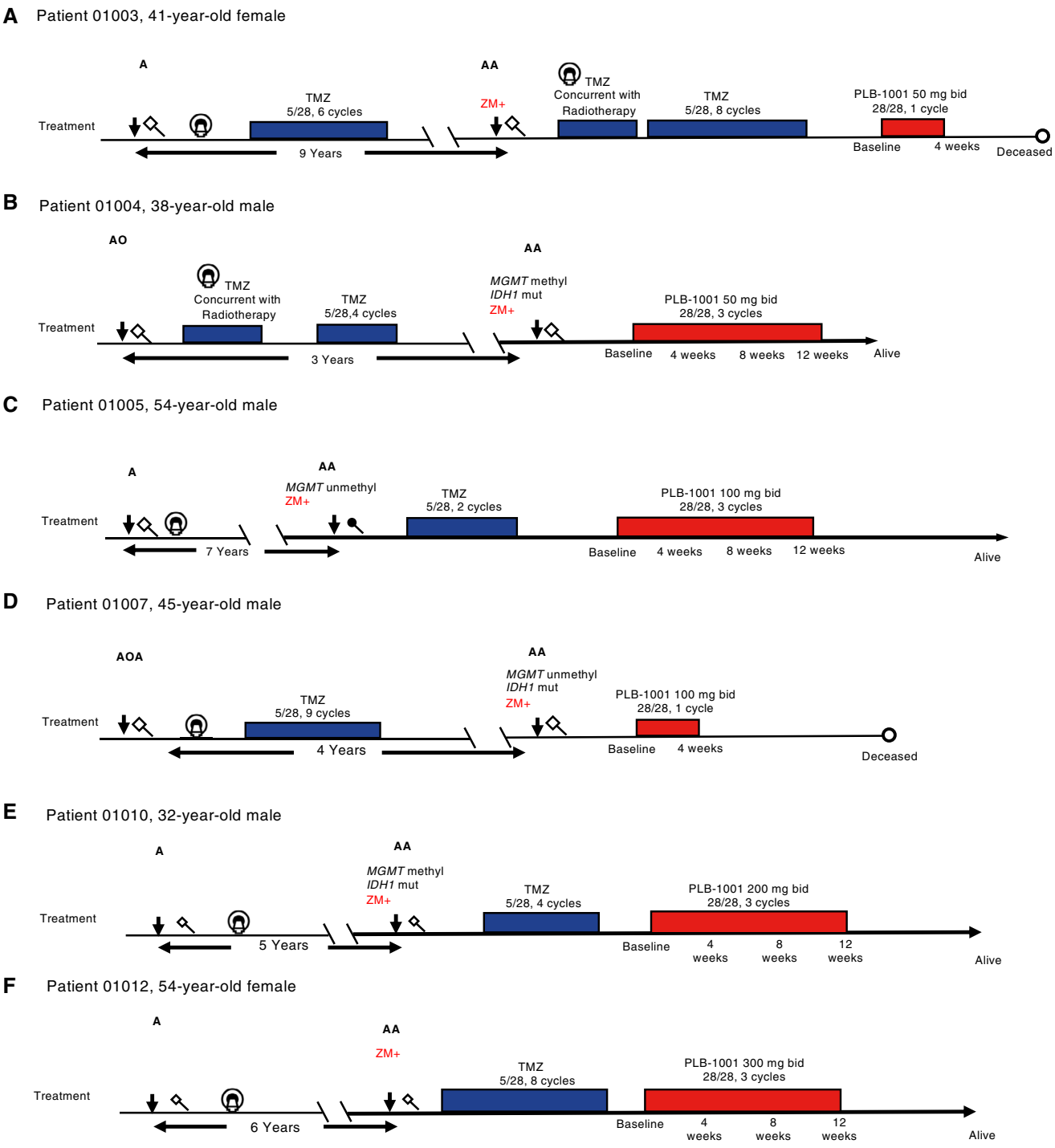

Figure S5. Clinical Records of Grade III Glioma Patients Enrolled in PLB-1001 Trial, Related to Figure 6

(A) Diagram of the glioma progression and treatment in patient P01003. Patient P01003 was a 41-year-old female, diagnosed with anaplastic astrocytoma (AA) after 9 years since the initial astrocytoma (A) was resected and treated with TMZ following radiotherapy. ZM fusion was detected in the AA sample. The patient was later subscribed with TMZ concurrent with radiotherapy followed by 8 cycles of TMZ and PLB-1001 treatment (50 mg bid), subsequently. MRI evaluation after 4 week of PLB-1001 treatment demonstrated increased tumor volume. The patient deceased with a 518-day PPS.

(B) Diagram of the glioma progression and treatment in patient P01004. Patient P01004 was a 38-year-old male, diagnosed with AA after 3 years since the initial anaplastic oligodendroglioma (AO) was resected and treated with TMZ concurrent with radiotherapy followed by 4 cycles of TMZ subsequently. ZM fusion was detected in the AA sample, and the patient was later subscribed with PLB-1001 treatment (50 mg bid). MRI evaluation after 12 weeks of PLB-1001 treatment demonstrated stable tumor volume. The patient is still alive with a 565-day PPS.

(legend continued on next page)

(C) Diagram of the glioma progression and treatment in patient P01005. Patient P01005 was a 54-year-old male with AA. Since the initial low grade A was treated with radiotherapy, the tumor recurred locally and progressed into AA. ZM fusion was detected in the AA sample, and the patient was later subscribed with 2 cycles of TMZ treatment followed by 3 cycles of PLB-1001 treatment (100 mg bid). MRI evaluation after 12 weeks of PLB-1001 treatment demonstrated stable tumor volume accompanied by symptom relief. The patient is still alive with a 492-day PPS.

(D) Diagram of the glioma progression and treatment in patient P01007. Patient P01007 was a 45-year-old male, diagnosed with AA after 4 years since the initial anaplastic oligodendroastrocytoma (AOA) was resected and treated with TMZ following radiotherapy. ZM fusion was detected in the AA sample, and the patient was later subscribed with PLB-1001 treatment (100 mg bid). MRI evaluation after 4 week of PLB-1001 treatment demonstrated increased tumor volume. The patient deceased with a 276-day PPS.

(E) Diagram of the glioma progression and treatment in patient P01010. Patient P01010 was a 32-year-old male, diagnosed with AA after 5 years since the initial A was resected and treated with radiotherapy. ZM fusion was detected in the AA sample. The patient was later subscribed with TMZ treatment followed by PLB-1001 treatment (200 mg bid), subsequently. MRI evaluation after 12 weeks of PLB-1001 treatment demonstrated a new recurrent lesion. The patient is still alive with a 445-day PPS.

(F) Diagram of the glioma progression and treatment in patient P01012. Patient P01012 was a 54-year-old female, diagnosed with AA after 6 years since the initial A was resected and treated with radiotherapy. ZM fusion was detected in the AA sample. The patient was later subscribed with 8 cycles of TMZ treatment followed by PLB-1001 treatment (300 mg bid). MRI evaluation after 12 weeks of PLB-1001 treatment demonstrated stable tumor volume. The patient is still alive with a 524-day PPS.

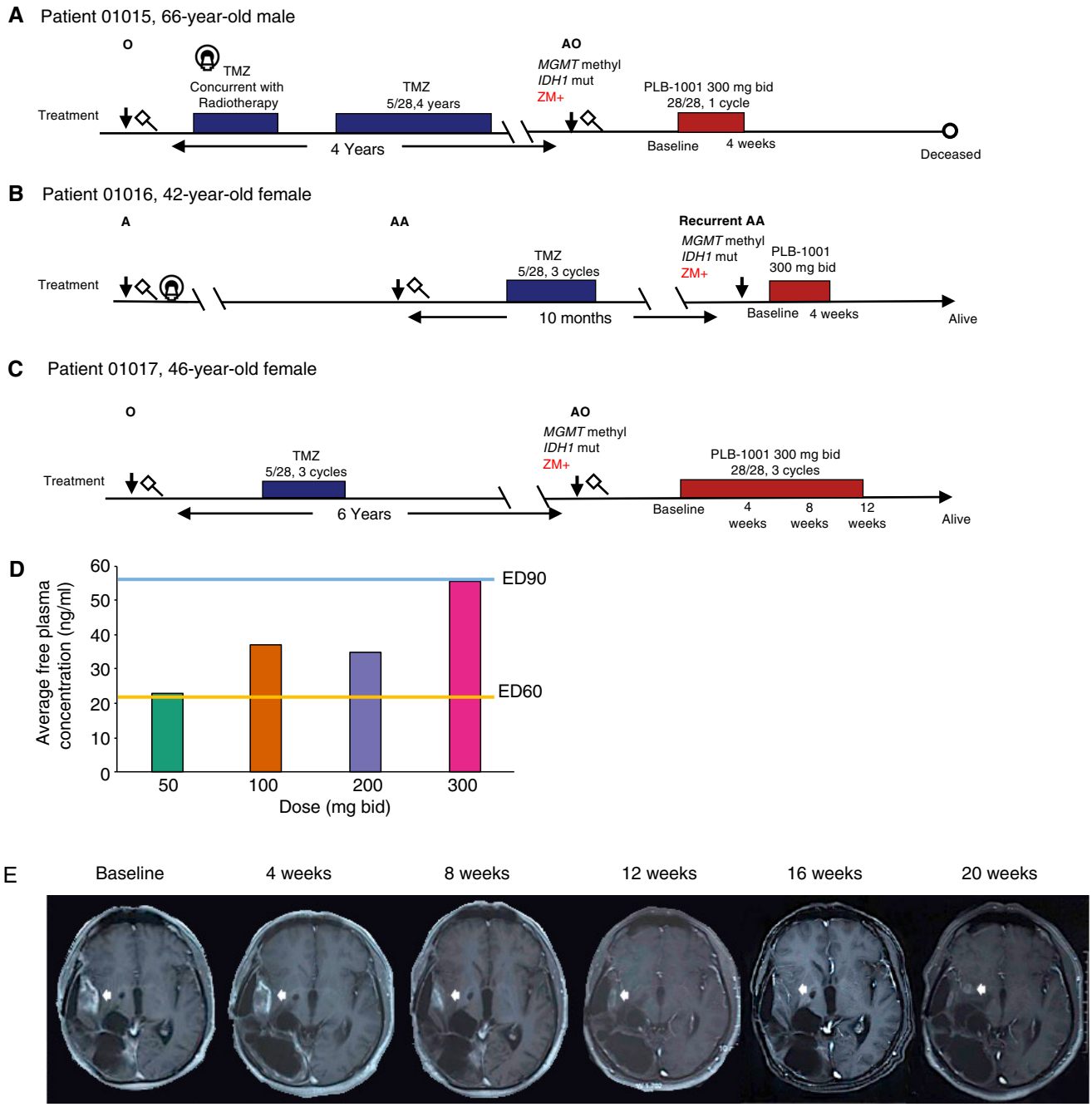

Figure S6. Additional Clinical Records of Grade III Glioma Patients Enrolled in PLB-1001 Trial and Characterization of Drug Concentration and Recurrence Mechanisms, Related to Figure 6

(A) Diagram of the glioma progression and treatment in patient P01015. Patient P01015 was a 66-year-old male, diagnosed with anaplastic oligodendroglioma (AO) after 4 years since the initial oligodendroglioma (O) was resected and treated with TMZ concurrent with radiotherapy, followed by 4 years of TMZ. ZM fusion was detected in the AO sample, and the patient was later subscribed with PLB-1001 treatment (300 mg bid). MRI evaluation after 4 weeks of PLB-1001 treatment demonstrated increased tumor volume. The patient deceased with a 150-day PPS.

(B) Diagram of the glioma progression and treatment in patient P01016. Patient P01016 was a 64-year-old male treated after 3 cycles of TMZ. After 7 years since the initial low-grade astrocytoma (A) was resected and treated with radiotherapy, the tumor recurred locally and progressed into anaplastic astrocytoma (AA). ZM fusion was detected in the recurrent sGBM sample, and the patient was later subscribed with PLB-1001 treatment (300 mg bid). MRI evaluation after 4 weeks of PLB-1001 treatment demonstrated increased tumor volume. The patient is still alive with a 164-day PPS.

(C) Diagram of the glioma progression and treatment in patient P01017. Patient P01017 was a 45-year-old female patient, diagnosed with AO after 6 years since the initial O was resected and treated with 3 cycles of TMZ. ZM fusion was detected in the AO sample, and the patient was later subscribed with PLB-1001 treatment (300 mg bid). MRI evaluation after 12 weeks of PLB-1001 treatment demonstrated stable tumor volume. The patient is still alive with a 194-day PPS.

(legend continued on next page)

(D) The mean free fraction for PLB-1001 in human blood was 1.2%. The average free plasma concentration was then calculated based on the total plasma concentration of patients in phase I clinical trial. The 60% effective dose (ED60) and 90% effective dose (ED90) were inferred from preclinical mouse model. Data was shown in Table S6.

(E) The tumor in Patient P01011 under PLB-1001 treatment was monitored by MRI evaluation every 4 weeks. The tumor was located on right temporal and insular lobe. We defined 1st MRI evaluation after PLB-1001 treatment as the baseline evaluation. MRI evaluation after 16 weeks of PLB-1001 treatment demonstrated decreased enhancement and tumor shrinkage accompanied by symptom relief. No radiological progression was detected until 20 weeks after PLB-1001. The location of tumor is marked by arrowhead.